

# An Application of WKBJ Theory for Triad Interactions of Internal Gravity Waves in Varying Background Flows

Georg S. Voelker<sup>1\*</sup> | T. R. Akylas<sup>2</sup> | Ulrich Achatz<sup>1</sup>

<sup>1</sup>Institute for Atmospheric and Environmental Sciences, Goethe University Frankfurt, Frankfurt, Germany

<sup>2</sup>Department of Mechanical Engineering, Massachusetts Institute of Technology, MA, USA

## Correspondence

G. S. Voelker, Institute for Atmospheric and Environmental Sciences, Goethe University Frankfurt, Frankfurt, Germany  
Email: voelker@iau.uni-frankfurt.de

## Funding information

German Research Foundation (DFG), Grant/Award Number: AC 71/8-2, AC 71/9-2, AC 71/10-2, AC 71/11-2, AC 71/12-2, and BO 5071/1-2; US National Science Foundation, Grant/Award Number: DMS-1512925

Motivated by the question of whether and how wave-wave interactions should be implemented into atmospheric gravity-wave parameterizations, the modulation of triadic gravity-wave interactions by a slowly varying and vertically sheared mean-flow is considered for a non-rotating Boussinesq fluid with constant stratification. An analysis using a multiple-scales WKBJ expansion identifies two distinct scaling regimes, a linear off-resonance regime, and a non-linear near-resonance regime. Simplifying the near-resonance interaction equations allows for the construction of a parametrization for the triadic energy exchange which has been implemented into a one-dimensional WKBJ ray-tracing code. Theory and numerical implementation are validated for test cases where two wave trains generate a third wave train while spectrally passing through resonance. In various settings, of interacting vertical wavenumbers, mean-flow shear, and initial wave amplitudes, the WKBJ simulations are generally in good agreement with wave-resolving simulations. Both stronger mean-flow shear and smaller wave amplitudes suppress the energy exchange among a resonantly interacting triad. Experiments with mean-flow shear as strong as in the vicinity of atmospheric jets suggest that internal grav-

---

**Abbreviations:** GW, gravity wave; WKBJ, Wentzel-Kramers-Brillouin-Jeffreys

\* Corresponding author.

ity wave dynamics are dominated in such regions by wave modulation. Yet, triadic gravity-wave interactions are likely to be relevant in weakly sheared regions of the atmosphere.

#### KEYWORDS

internal gravity waves; wave modulation; triadic wave-wave interaction; parametrization; ray-tracing

## 1 | INTRODUCTION

Internal gravity waves (GWs) are an important mode of atmospheric dynamics, transporting energy and momentum over large distances from generation regions to regions of dissipation, thereby significantly influencing the atmospheric circulation, especially in the middle atmosphere (Fritts and Alexander, 2003; Kim et al., 2003; Plougonven and Zhang, 2014). Being too small in scale to be fully resolvable by present-day weather-forecast and climate codes, GWs constitute an important aspect of the parameterization problem in these models. Their spectrum is influenced to a considerable degree by modulation by a spatially and time dependent resolved flow (Bretherton, 1966; Eckermann and Marks, 1997; Senf and Achatz, 2011). Especially at large vertical wavenumbers the observed GW spectrum exhibits a slope, somewhat independent of time and location (Dewan and Good, 1986; Smith et al., 1987; Fritts and Vanzandt, 1993), which is reminiscent of the quasi-universal spectrum GWs are often thought to exhibit in the ocean (Garrett and Munk, 1972, 1975; Polzin and Lvov, 2011). The universality of that spectrum is considered an indication of a transfer of energy in wavenumber (e.g. Olbers and Eden, 2013), usually attributed to nonlinear wave-wave interactions (Olbers, 1976; McComas and Bretherton, 1977; Pomphrey et al., 1980; Mueller et al., 1986; Lvov and Tabak, 2001; Lvov et al., 2004). Wave-turbulence theory (Hasselmann, 1962, 1966; Caillol and Zeitlin, 2000; Nazarenko, 2011; Eden et al., 2019) is a well-established tool for studies of corresponding spectra, considering statistical ensembles of GW fields, that most often focus on resonant triad interactions. In all of these the influence of mean-flow shear and varying stratification are neglected.

A complementary approach is WKB theory (Bretherton, 1966; Grimshaw, 1975; Achatz et al., 2010, 2017) which, instead of considering continuous wave-spectra, describes the development of locally monochromatic GW fields

20 which feature a nearly discrete spectrum. Moreover the WKB approach takes into account nonlinear interactions  
21 between GWs and a spatially and temporally varying mean flow. WKB theory is the basis of present-day GW pa-  
22 rameterizations, however, for most applications relying on a steady-state approximation where GWs instantaneously  
23 assume an equilibrium distribution defined by the available sources and the mean flow (Kim et al., 2003; Kim et al.,  
24 2020; Quinn et al., 2020). While the GWs are modulated by the mean flow in this approximation, a GW impact on  
25 the mean flow is only possible once GWs dissipate, e.g. by wave breaking. Non-dissipative direct GW-mean-flow in-  
26 teractions, relying on explicit GW transience, can only be described once the steady-state approximation is dropped.  
27 In numerical implementations this tends to lead to instabilities due to caustics (e.g. Rieper et al., 2013a) that can be  
28 avoided, however, when WKB theory is translated into a spectral formulation (Muraschko et al., 2015). Using this  
29 approach Bölöni et al. (2016) have shown that direct, non-dissipative GW-mean-flow interactions dominate over dis-  
30 sipative effects in the dynamics of upward propagating GW packets and the wind induced by them. Hence it seems  
31 appropriate to generalize GW parameterizations accordingly.

32 Many process studies have investigated GW-GW interactions in the atmosphere (e.g. Dong and Yeh, 1988, 1991;  
33 Fritts et al., 1992; Yi and Xiao, 1997; Huang et al., 2007). However, these have not alleviated the obvious deficiency  
34 of WKB-based GW parameterizations that they do not take such interactions into account (Kim et al., 2003). Shear  
35 effects are not of leading-order importance in the ocean (e.g. Garrett and Munk, 1972, 1975; Mueller, 1976; Elipot  
36 et al., 2010), so there it seems appropriate to just supplement the spectral wave-action equation resulting from WKB  
37 by nonlinear scattering integrals as derived from a wave-turbulence theory (e.g. Olbers and Eden, 2013) assuming a  
38 zero or constant large-scale flow. In the atmosphere, however, it appears that the modulation of GWs by the large-  
39 scale flow is the dominant effect, so that a consistent numerical treatment of GW propagation through a sheared  
40 environment, while simultaneously undergoing wave-wave interactions, seems to be more important. Once a numer-  
41 ical implementation of a corresponding theory were available, one could better investigate the relevance of GW-GW  
42 interactions in the atmosphere as such. So far it seems to be unclear whether the typical life time of an atmospheric  
43 GW, between emission from its source and its turbulent breaking, gives nonlinear triad interactions enough room to  
44 act. If so, consecutive wave-wave interactions, i.e. wave turbulence, could be an efficient mechanism for the nonlinear  
45 dissipation itself. Furthermore an interesting question in this context is how much triad interactions are affected by

46 wave modulation due to varying large-scale flows. Such modulation changes GW wavenumber and frequency so that  
47 a triad might be brought into and out of resonance. Hence strongly sheared environments might actually suppress  
48 nonlinear interactions, while such interactions, as described by wave-turbulence theory, might be more effective in  
49 less sheared locations of the atmosphere.

50 With this motivation in mind, the work reported here builds on the study of Grimshaw (1988), who proposed a  
51 WKBJ theory for wave-wave interactions modulated by a slowly varying background flow. He considered the effect  
52 of the mean-flow shear on near-resonant triad interactions of internal gravity waves and outlined a possible approach  
53 to computing asymptotically the energy exchanges among the members of a triad that passes through resonance.  
54 The focus of the present study is the first (to our knowledge) implementation of such local resonant triad interactions  
55 into a numerical WKBJ model. In particular, we revisit the theory introduced by Grimshaw (1988) (Sections 2 to 4),  
56 simplify the equations to a quasi one dimensional setting (Section 5), and propose an interaction parameterization  
57 which allows for a straight forward application of the local interaction equations to the WKBJ modulation equations  
58 (Section 6). As an efficient tool for modeling the WKBJ equation system we use the spectral ray-tracing algorithm  
59 introduced by Muraschko et al. (2015) and expand it by a triad-interaction module. The resulting model is verified by  
60 constructing test cases of two interacting wave trains that generate a third wave train in the presence of a shear flow,  
61 and comparing the WKBJ simulations against wave-resolving simulations (Section 7). In general wave modulation by  
62 a variable background stratification or a sheared mean-flow are equally important in the atmosphere (cf. Achatz et al.,  
63 2017). However, we restrict the analysis to the case of Boussinesq dynamics with a constant background stratification  
64 and zero rotation for the sake of simplicity.

## 65 2 | FLOW REGIMES, NON-DIMENSIONALIZATION AND SCALING ASSUMP- 66 TIONS

67 We consider the non-rotating inviscid Boussinesq equations,

$$D_t \mathbf{v} = -\nabla p + \mathbf{e}_z b \quad (1)$$

$$D_t b = -N^2 w \quad (2)$$

$$0 = \nabla \cdot \mathbf{v} \quad (3)$$

68 where  $\mathbf{v} = (u, v, w)^T$ ,  $p$ ,  $b$ , and  $N$  denote the velocity vector, the pressure, the buoyancy, and the buoyancy frequency  
69 associated to the background stratification, respectively. Note that we have scaled the pressure with the reference  
70 density so that it does not appear in the equations. For convenience we denote the horizontal velocity vector as  
71  $\mathbf{u} = (u, v, 0)^T$ . The material derivative,  $D_t$ , is defined by  $D_t = \partial_t + \mathbf{v} \cdot \nabla$ . We non-dimensionalize the governing  
72 equations with the help of the scaling parameters summarized in Table 1 and some additional assumptions. Namely,  
73 (i) the horizontal and vertical scales are approximately equal

$$\tilde{H} \sim \tilde{L}$$

**TABLE 1** Summary of all scaling parameters.

name	symbol	name	symbol
temporal scale	$\bar{T}$	horizontal scale	$\bar{L}$
buoyancy frequency	$\tilde{N}$	vertical scale	$\tilde{H} = \bar{L}$
horizontal velocity	$\tilde{U} = \frac{\bar{L}}{\bar{T}}$	buoyancy	$\tilde{B} = \tilde{H} \tilde{N}^2$
vertical velocity	$\tilde{W} = \frac{\tilde{H}}{\bar{T}}$	pressure	$\tilde{P} = \tilde{B} \tilde{H}$

74 and (ii) the buoyancy and pressure are scaled such that the order  $O(1)$  represents the margin of static stability of  
 75 internal gravity waves

$$\tilde{B} = \bar{L} \tilde{N}^2$$

$$\tilde{P} = \tilde{B} \bar{L} = \bar{L}^2 \tilde{N}^2$$

76 Note that in this scaling regime rotation is a higher order effect and is set to zero for simplicity. Thus, the non-  
 77 dimensionalized governing equations for non-hydrostatic internal gravity waves in non-rotating Boussinesq dynamics  
 78 are given by

$$D_t \hat{\mathbf{v}} = -\nabla \hat{p} + e_z \hat{b} \quad (4)$$

$$D_t \hat{b} = -\hat{N}^2 \hat{w} \quad (5)$$

$$0 = \nabla \cdot \hat{\mathbf{v}} \quad (6)$$

79 Here, the hatted variables denote the non-dimensional variables. Unless indicated otherwise we will consider the  
 80 non-dimensional variables without explicitly denoting the hat in the course of this study. Moreover we introduce a  
 81 small parameter  $\epsilon$  to scale the wave modulation and strength of the nonlinearities. To establish a consistent balance  
 82 between modulation and nonlinearity we follow a WKBJ approach with weak wave amplitudes of order  $O(\epsilon)$  and

83 thus seek solutions of the form

$$y(x, t) = \sum_{k=0}^{\infty} e^k Y_0^{(k)}(T_1, T_2, \mathbf{X}_1, \mathbf{X}_2) + \Re \sum_{\beta} \sum_{n=1}^{\infty} \epsilon^n e^{i\phi_{\beta}(T_2, \mathbf{X}_2)/\epsilon^2} Y_{\beta}^{(n)}(T_1, T_2, \mathbf{X}_1, \mathbf{X}_2) \quad (7)$$

84 with  $y$  representing any of the fields  $v$ ,  $p$  or  $b$ . The first term above is an expansion of the large-scale flow in terms of  
 85 the scale-separation and wave-amplitude parameter,  $\epsilon$ , while the second constitutes the wave field. The compressed  
 86 coordinates,  $(T_n, \mathbf{X}_n)$ , are defined by  $(T_n, \mathbf{X}_n) = (\epsilon^n t, \epsilon^n \mathbf{x})$ . In doing so we introduce a three-scale system where  
 87 the fast scales,  $(T_0, \mathbf{X}_0)$ , correspond to the wave oscillations and the slow scales,  $(T_2, \mathbf{X}_2)$ , correspond to the slow  
 88 variation of the mean flow which in turn causes a slow modulation of the wave fields. The intermediate scales,  $(T_1, \mathbf{X}_1)$ ,  
 89 as explained below, are associated with the nonlinear wave-wave interaction. Choosing a wave field with leading order  
 90  $O(\epsilon)$  we balance the strength of the nonlinear terms with the modulation (Grimshaw, 1988; Glebov et al., 2005). The  
 91 summation over the index  $\beta$  represents the superposition of several wave trains in the solution. Moreover, for each  
 92 wave train, we define the wave frequency,  $\omega_{\beta}$ , and wave vector,  $\mathbf{k}_{\beta} = (k_{\beta}, l_{\beta}, m_{\beta})$ , as compressed temporal and spatial  
 93 derivatives of the wave phase,  $\phi_{\beta}$ , so that

$$\omega_{\beta}(T_2, \mathbf{X}_2) = -\partial_{T_2} \phi_{\beta} \qquad \mathbf{k}_{\beta}(T_2, \mathbf{X}_2) = \nabla_2 \phi_{\beta} \quad (8)$$

94 where the subscript indicates the scale of the derivative, i.e.  $\nabla_2 = (\partial_{X_2}, \partial_{Y_2}, \partial_{Z_2})^T$ . We hence construct wave solutions  
 95 with slowly varying amplitudes, wavenumbers and frequencies on the compressed scales  $(T_2, \mathbf{X}_2)$ .

96 It should be noted that for a superposition of wave trains with slowly varying amplitudes, the various harmonics  
 97 may be separated and the equations may be written for the individual wave trains, only if the corresponding fre-  
 98 quencies and wavenumbers are sufficiently separated. In particular the frequency difference of any two wave trains  
 99 must be at least  $\omega_{\beta} - \omega_{\gamma} \sim O(1)$ . A rigorous treatment may be done with the aid of the weak asymptotic method as

100 introduced by Danilov (2001).

101 Following similar arguments, the quadratic nonlinear terms are only important where the conditions for a resonant  
 102 triad are satisfied or nearly so. The behavior is then analogous to the spectral passage through resonance of harmonic  
 103 oscillators (Neu, 1983). In the case of an isolated triad the quadratic nonlinearities scale with an exponential phase  
 104 factor  $e^{i\Delta\phi/\epsilon^2}$ , where the phase difference is defined as  $\Delta\phi = \pm\phi_\gamma \pm \phi_\delta - \phi_\beta$  with signs depending on the various triad  
 105 combinations (cf. Grimshaw, 1988). In the case of an exact and static, i.e. time independent, resonance one finds  
 106  $\Delta\phi \equiv 0$  such that the phase factor becomes unity. In terms of wave vectors and frequencies that is,

$$-\partial_{T_2} \Delta\phi = \pm\omega_\gamma \pm \omega_\delta - \omega_\beta = 0 \quad (9)$$

$$\nabla_2 \Delta\phi = \pm k_\gamma \pm k_\delta - k_\beta = 0 \quad (10)$$

107 These are the the well-known resonance conditions of the classical interaction with constant stratification and zero  
 108 background. If the resonance is, however, not exactly satisfied or the phase difference is a function of time and space  
 109 due to wave modulation the phase factor enters the nonlinear interaction equations. For visualization of the local  
 110 scaling we locally expand the phase difference,  $\Delta\phi$ , in the compressed time. In particular one finds

$$\frac{\Delta\phi}{\epsilon^2} \approx \left(\frac{\Delta\phi}{\epsilon^2}\right)_0 + (\partial_{T_2} \Delta\phi)_0 T_0 + \frac{1}{2} (\partial_{T_2}^2 \Delta\phi)_0 T_1^2 = \left(\frac{\Delta\phi}{\epsilon^2}\right)_0 - (\Delta\omega)_0 T_0 - \frac{1}{2} (\partial_{T_2} \Delta\omega)_0 T_1^2 \quad (11)$$

111 Thus the typical exponential term,  $e^{i\Delta\phi/\epsilon^2}$ , due to quadratic nonlinearities is oscillating with the fast time scale,  $T_0$ , in  
 112 general but becomes a function of the intermediate time scale,  $T_1$ , near resonance. The latter is the case as long as  
 113  $T_1 \sim O(1)$  and hence  $\Delta\omega = \partial\Delta\phi/\partial T_2 \sim O(\epsilon)$ . Consequently the quadratic nonlinear terms are important only in an  
 114  $\epsilon$ -neighborhood around resonance (Grimshaw, 1988). A similar argument can be employed in all spatial dimensions  
 115 such that one may obtain an analogous condition for the wavenumbers,  $\Delta k \sim O(\epsilon)$ .



116 We thus follow Grimshaw (1988) and Glebov et al. (2005), and consider two distinct regimes: the linear off-  
 117 resonance solution, where the nonlinear triad terms can be neglected, and the weakly nonlinear near-resonance so-  
 118 lution.

### 119 3 | THE LINEAR OFF-RESONANT SOLUTION

120 As long as the nonlinear terms do not come into play, the off-resonance solution is equivalent to the classical linear  
 121 internal-gravity-wave theory, and all fields depend on the slow coordinates,  $(T_2, \mathbf{X}_2)$ , only. Consequently the resulting  
 122 equation hierarchy is equivalent to the well-known linear WKBJ theory for non-hydrostatic internal gravity waves  
 123 (e.g. Achatz et al., 2010; Sutherland, 2010). Therefore we will only briefly review the most important results here,  
 124 obtained after inserting (7) into Eqs. (4) to (6) and sorting in terms of powers of  $\epsilon$  and the phase factor.

#### 125 3.1 | Leading Order Mean Flow Evolution

126 In view of the assumptions of Boussinesq dynamics and weak wave amplitudes, the leading-order mean-flow velocity  
 127 is purely horizontal and incompressible

$$\mathbf{V}_0^{(0)} = \mathbf{U}_0^{(0)} \qquad 0 = \nabla_2 \cdot \mathbf{V}_0^{(0)} \qquad (12)$$

128 Furthermore it is governed by

$$0 = (\partial_{T_2} + \mathbf{U}_0^{(0)} \cdot \nabla_2) \mathbf{U}_0^{(0)} + \nabla_2 P_0^{(0)} - e_z B_0^{(2)} \qquad (13)$$

129 Hence the leading-order horizontal mean-flow is independent of the wave field. Moreover, we find that  $B_0^{(0)} = B_0^{(1)} =$   
 130 0, and that the leading-order mean-flow pressure,  $P_0^{(0)}$ , and the leading-order buoyancy,  $B_0^{(2)}$ , are in hydrostatic bal-  
 131 ance. We also obtain  $W_0^{(0)} = W_0^{(1)} = W_0^{(2)} = W_0^{(3)} = 0$ , and with this the evolution of the leading-order buoyancy is  
 132 given by

$$0 = (\partial_{\tau_2} + \mathbf{U}_0^{(0)} \cdot \nabla_2) B_0^{(2)} + N^2 W_0^{(4)} \quad (14)$$

133 and therefore linked to the leading-order vertical mean wind,  $W_0^{(4)}$ .

### 134 3.2 | Dispersion and Polarization Relations

135 The internal gravity wave evolution is characterized by the following dispersion relation (e.g. Sutherland, 2010)

$$\hat{\omega}_\beta^2 = \frac{N^2 (k_\beta^2 + l_\beta^2)}{k_\beta^2 + l_\beta^2 + m_\beta^2} \quad (15)$$

136 with the intrinsic frequency,  $\hat{\omega}_\beta = \omega_\beta - \mathbf{k}_\beta \cdot \mathbf{U}_0^{(0)}$ . The polarization relations are

$$\mathbf{Z}_\beta^{(1)} = \left( U_\beta^{(1)}, V_\beta^{(1)}, W_\beta^{(1)}, \frac{B_\beta^{(1)}}{N}, P_\beta^{(1)} \right)^T = W_\beta^{(1)} \left( -\frac{k_\beta m_\beta}{k_\beta^2 + l_\beta^2}, -\frac{l_\beta m_\beta}{k_\beta^2 + l_\beta^2}, 1, \frac{N}{i \hat{\omega}_\beta}, -\frac{m_\beta \hat{\omega}_\beta}{k_\beta^2 + l_\beta^2} \right)^T \quad (16)$$

137 Note that we restrict our analysis to the internal gravity wave evolution and neglect the vortical mode corresponding to  
 138 the solution  $\hat{\omega}_\beta = 0$ . The next-order wave equations reveal that the next-order mean-flow velocities vanish, i.e.  $\mathbf{U}_0^{(1)} \equiv$   
 139 0.

### 140 3.3 | The Eikonal Equations

141 We use the standard definition for the group velocities corresponding to the extrinsic and intrinsic frequencies

$$\nabla_{\mathbf{k}_\beta} \omega_\beta = \mathbf{c}_{g,\beta} \qquad \nabla_{\mathbf{k}_\beta} \hat{\omega}_\beta = \hat{\mathbf{c}}_{g,\beta} \qquad (17)$$

142 where  $\nabla_{\mathbf{k}_\beta}$  denotes the derivatives with respect to the corresponding wavenumbers  $\nabla_{\mathbf{k}_\beta} = (\partial_{k_\beta}, \partial_{l_\beta}, \partial_{m_\beta})^T$ . Using the  
143 dispersion relation (Eq. 15) one may derive the evolution of the frequencies and wavenumbers - the eikonal equations.

144 Specifically,

$$(\partial_{\tau_2} + \mathbf{c}_{g,\beta} \cdot \nabla_2) \omega_\beta = \mathbf{k}_\beta \cdot \partial_{\tau_2} \mathbf{U}_0^{(0)} \qquad (18)$$

$$(\partial_{\tau_2} + \mathbf{c}_{g,\beta} \cdot \nabla_2) \mathbf{k}_\beta = -\mathbf{k}_\beta (\nabla_2 U_0^{(0)}) - l_\beta (\nabla_2 V_0^{(0)}) \qquad (19)$$

145 where the explicit form of the intrinsic group velocity,  $\hat{\mathbf{c}}_{g,\beta}$ , and the extrinsic group velocity,  $\mathbf{c}_{g,\beta}$ , are given by

$$\hat{\mathbf{c}}_{g,\beta} = \frac{\hat{\omega}_\beta^3}{N^2} \frac{m_\beta}{k_\beta^2 + l_\beta^2} \left( \frac{k_\beta m_\beta}{k_\beta^2 + l_\beta^2}, \frac{l_\beta m_\beta}{k_\beta^2 + l_\beta^2}, -1 \right)^T = \mathbf{c}_{g,\beta} - \mathbf{U}_0^{(0)} \qquad (20)$$

### 146 3.4 | Wave Action Conservation

147 The linear wave action conservation in standard form is

$$0 = \partial_{T_2} \mathcal{A}_\beta + \nabla_2 \cdot (c_{g,\beta} \mathcal{A}_\beta) \quad (21)$$

148 where the wave action,  $\mathcal{A}_\beta$ , is defined as the ratio of the wave energy and corresponding intrinsic frequency,  $\mathcal{A}_\beta =$

149  $E_\beta / \hat{\omega}_\beta$ , where

$$E_\beta = \frac{1}{2} \frac{N^2}{\hat{\omega}_\beta^2} |W_\beta^{(1)}|^2 \quad (22)$$

### 150 3.5 | Wave Impact on the Mean Flow and Leading-Order Vertical Winds

151 Exploiting higher orders one may find that the second-order horizontal mean flow,  $U_0^{(2)}$ , the next-order buoyancy,  
 152  $B_0^{(3)}$ , and the leading-order vertical wind,  $W_0^{(4)}$ , are directly interacting with the wave field. Moreover, the leading-  
 153 order vertical mean flow is connected to the leading-order buoyancy by Eq. (14) and therefore affects the hydrostatic  
 154 relation. However, the leading-order vertical mean flow is three orders smaller compared to the leading-order wave  
 155 amplitude,  $W_\beta^{(1)}$ . Also, there is no feedback onto the wave field. Thus the wave impact onto the mean flow will be  
 156 treated as a higher order effect and will not be taken into account here, in accordance with the weak-wave-amplitude  
 157 assumption.

## 158 4 | THE NONLINEAR NEAR-RESONANCE SOLUTION

159 The near-resonance solution hinges on the quadratic triad terms and depends on the intermediate-scale coordinates  
 160  $(T_1, \mathbf{X}_1)$ . Hence the wave amplitudes and second- as well as higher-order mean flow also vary on the intermediate  
 161 scales. The leading-order mean-flow contributions are assumed to depend on the slow coordinates,  $(T_2, \mathbf{X}_2)$ , only,  
 162 as they correspond to the slowly varying background and wave modulation. We next derive the asymptotic hierarchy  
 163 closely following Grimshaw (1988) and Achatz et al. (2010).

### 164 4.1 | Leading-Order Mean-Flow Evolution

165 Similarly to the off-resonance solution, the horizontal mean flow and pressure are of order  $O(1)$ ,  $\mathbf{U}_0^{(0)} = \mathbf{U}_0^{(0)}(T_2, \mathbf{X}_2)$   
 166 and  $P_0^{(0)} = P_0^{(0)}(T_2, \mathbf{X}_2)$ . They represent the slowly varying background state and are therefore assumed to be  
 167 dependent on the slow scales only. Also the leading-order mean-flow buoyancy,  $B_0^{(2)}$ , and leading-order vertical  
 168 wind,  $W_0^{(4)}$ , are of order  $O(\epsilon^2)$  and  $O(\epsilon^4)$ , respectively. We thus set  $B_0^{(2)} = B_0^{(2)}(T_2, \mathbf{X}_2)$ .

169 The leading-order incompressibility criterion requires that

$$0 = \nabla_2 \cdot \mathbf{U}_0^{(0)} + \nabla_1 \cdot \mathbf{U}_0^{(1)} \quad (23)$$

170 Averaging Eq. (23) over the intermediate scales, and requiring sub-linear growth of  $\nabla_1 \cdot \mathbf{U}_0^{(1)}$  so that  $0 = \overline{\nabla_1 \cdot \mathbf{U}_0^{(1)}}^{(T_1, \mathbf{X}_1)}$ ,  
 171 we find that the leading and next-order mean-flow velocities,  $\mathbf{U}_0^{(0)}$  and  $\mathbf{U}_0^{(1)}$ , are incompressible

$$0 = \nabla_2 \cdot \mathbf{U}_0^{(0)} \quad 0 = \nabla_1 \cdot \mathbf{U}_0^{(1)} \quad (24)$$

172 The evolution of the leading-order horizontal mean flow is given by

$$0 = (\partial_{T_2} + \mathbf{U}_0^{(0)} \cdot \nabla_2) \mathbf{U}_0^{(0)} + \nabla_2 P_0^{(0)} - e_z B_0^{(2)} + (\partial_{T_1} + \mathbf{U}_0^{(0)} \cdot \nabla_1) \mathbf{U}_0^{(1)} + \nabla_1 P_0^{(1)} \quad (25)$$

173 Again one may average Eq. (25) over the intermediate scales and obtains, via the sub-linear growth assumption,  $0 =$

$$174 \overline{\partial_{T_1} \mathbf{U}_0^{(1)}}^{(T_1, \mathbf{X}_1)} \text{ as well as } 0 = \overline{(\mathbf{U}_0^{(0)} \cdot \nabla_1) \mathbf{U}_0^{(1)}}^{(T_1, \mathbf{X}_1)} = \overline{\nabla_1 P_0^{(1)}}^{(T_1, \mathbf{X}_1)}. \text{ One then finds that Eq. (25) can be separated}$$

175 so that

$$0 = (\partial_{T_2} + \mathbf{U}_0^{(0)} \cdot \nabla_2) \mathbf{U}_0^{(0)} + \nabla_{2,h} P_0^{(0)} \quad (26)$$

$$0 = (\partial_{T_1} + \mathbf{U}_0^{(0)} \cdot \nabla_1) \mathbf{U}_0^{(1)} + \nabla_{1,h} P_0^{(1)} \quad (27)$$

$$0 = \partial_{Z_2} P_0^{(0)} - e_z B_0^{(2)} \quad (28)$$

$$0 = \partial_{Z_1} P_0^{(1)} \quad (29)$$

176 where Eq. (28) represents the hydrostatic balance of the mean flow to leading order. Thus the evolution of the leading-

177 order mean flow is equivalent to the linear regime (Eq. 13). The leading-order mean-flow buoyancy evolves as

$$0 = (\partial_{T_2} + \mathbf{U}_0^{(0)} \cdot \nabla_2) B_0^{(2)} + N^2 \overline{W_0^{(4)}}^{(T_1, \mathbf{X}_1)} \quad (30)$$

178 Leading-order mean-flow buoyancy and vertical mean wind are therefore linked similarly to the linear regime. Even

179 though we may neglect the small leading-order vertical mean flow we will use this statement to obtain the formal

180 leading-order matching conditions for the two regimes.

## 181 4.2 | Dispersion, Polarization, and Interaction Equations

182 Due to the small wave amplitudes the dispersion relation as well as the polarization relations are retained from the  
 183 linear evolution (cf. Eqs. 15 and 16). In contrast to the off-resonance solution, the wave amplitude and wave action  
 184 equations comprise the nonlinear triad terms. Projecting the next-order wave evolution equations onto the normalized  
 185 polarization relations (cf. Achatz et al., 2010) one arrives at the wave amplitude equation,

$$\begin{aligned}
 0 = & (\partial_{T_1} + \mathbf{c}_{\mathbf{g},\beta} \cdot \nabla_1) W_\beta^{(1)} + i(\mathbf{U}_0^{(1)} \cdot \mathbf{k}_\beta) W_\beta^{(1)} \\
 & + \sum_{\gamma,\delta} e^{i(\phi_\gamma + \phi_\delta - \phi_\beta)/\varepsilon^2} A_{\beta\gamma\delta}^+ W_\gamma^{(1)} W_\delta^{(1)} + \sum_{\gamma,\delta} e^{i(-\phi_\gamma - \phi_\delta - \phi_\beta)/\varepsilon^2} A_{\beta\gamma\delta}^- W_\gamma^{(1)*} W_\delta^{(1)*} \\
 & + \sum_{\gamma \neq \delta} e^{i(\phi_\gamma - \phi_\delta - \phi_\beta)/\varepsilon^2} A_{\beta\gamma\delta}^- W_\gamma^{(1)} W_\delta^{(1)*} + \sum_{\gamma \neq \delta} e^{i(-\phi_\gamma + \phi_\delta - \phi_\beta)/\varepsilon^2} A_{\beta\gamma\delta}^+ W_\gamma^{(1)*} W_\delta^{(1)*}
 \end{aligned} \tag{31}$$

186 with the interaction coefficients (cf. McEwan and Plumb, 1977)

$$A_{\beta\gamma\delta}^\pm = \pm i \frac{1}{4} \frac{\hat{\omega}_\beta^2}{N^2} \left( m_\delta - m_\gamma \frac{k_\delta k_\gamma + l_\delta l_\gamma}{k_\gamma^2 + l_\gamma^2} \right) \left[ \frac{m_\beta m_\delta (k_\beta k_\delta + l_\beta l_\delta)}{(k_\beta^2 + l_\beta^2)(k_\delta^2 + l_\delta^2)} + 1 \pm \frac{N^2}{\hat{\omega}_\delta \hat{\omega}_\beta} \right] \tag{32}$$

187 The wave action evolution then follows as

$$0 = \partial_{T_1} \mathcal{A}_\beta + \nabla_1 \cdot (\mathbf{c}_{\mathbf{g},\beta} \mathcal{A}_\beta) + T_\beta^{(1)} \tag{33}$$

188 with the wave action,  $\mathcal{A}_\beta$ , being defined analogous to the linear solution (cf. Eq. 22). Here, the interaction term,  $T_\beta^{(1)}$ ,

189 is given by

$$\begin{aligned}
 T_{\beta}^{(1)} &= \sum_{\gamma, \delta} e^{i(\phi_{\gamma} + \phi_{\delta} - \phi_{\beta})/\epsilon^2} \frac{1}{2} \frac{N^2}{\hat{\omega}_{\beta}^3} A_{\beta\gamma\delta}^{+} W_{\gamma}^{(1)} W_{\delta}^{(1)} W_{\beta}^{(1)*} \\
 &+ \sum_{\gamma, \delta} e^{i(-\phi_{\gamma} - \phi_{\delta} - \phi_{\beta})/\epsilon^2} \frac{1}{2} \frac{N^2}{\hat{\omega}_{\beta}^3} A_{\beta\gamma\delta}^{-} W_{\gamma}^{(1)*} W_{\delta}^{(1)*} W_{\beta}^{(1)*} \\
 &+ \sum_{\gamma \neq \delta} e^{i(\phi_{\gamma} - \phi_{\delta} - \phi_{\beta})/\epsilon^2} \frac{1}{2} \frac{N^2}{\hat{\omega}_{\beta}^3} A_{\beta\gamma\delta}^{-} W_{\gamma}^{(1)} W_{\delta}^{(1)*} W_{\beta}^{(1)*} \\
 &+ \sum_{\gamma \neq \delta} e^{i(-\phi_{\gamma} + \phi_{\delta} - \phi_{\beta})/\epsilon^2} \frac{1}{2} \frac{N^2}{\hat{\omega}_{\beta}^3} A_{\beta\gamma\delta}^{+} W_{\gamma}^{(1)*} W_{\delta}^{(1)} W_{\beta}^{(1)*} \tag{34}
 \end{aligned}$$

190 Thus in the near-resonance solution wave action is conserved up to the exchange of energy between the modes. Note  
 191 that due to the cubic nonlinearities, that is  $T_{\beta}^{(1)} \sim W_{\gamma}^{(1)} W_{\delta}^{(1)} W_{\beta}^{(1)*}$  (and complex conjugates), Eq. (33) is ill posed when  
 192 the amplitude,  $W_{\beta}^{(1)}$ , is initially zero (cf. Eq. 22). Instead it is necessary to solve the amplitude equation (Eq. 31) near  
 193 resonance.

### 194 4.3 | Energy Conservation

195 Naturally the linear solution comprises the wave-action conservation (Eq. 21). Near resonance, while the wave action  
 196 of each wave train is not conserved, wave triads exchange energy such that the sum of all wave energies is conserved.  
 197 Therefore one may assess the total energy balance by considering an individual triad with resonance conditions

$$\mathbf{k}_1 = \mathbf{k}_2 + \mathbf{k}_3 \tag{35}$$

$$\hat{\omega}_1 = \hat{\omega}_2 + \hat{\omega}_3 \tag{36}$$



198 The evolution of the corresponding wave energies is then given by the three coupled equations

$$0 = \partial_{T_1} E_1 + \nabla_1 \cdot (c_{g,1} E_1) + \Re \left[ e^{i(\phi_2 + \phi_3 - \phi_1)/\epsilon^2} \frac{1}{2} \frac{N^2}{\hat{\omega}_1^2} (A_{123}^+ + A_{132}^+) W_1^{(1)*} W_2^{(1)} W_3^{(1)} \right] \quad (37)$$

$$0 = \partial_{T_1} E_2 + \nabla_1 \cdot (c_{g,2} E_2) - \Re \left[ e^{i(\phi_2 + \phi_3 - \phi_1)/\epsilon^2} \frac{1}{2} \frac{N^2}{\hat{\omega}_2^2} (A_{213}^- + A_{231}^+) W_1^{(1)*} W_2^{(1)} W_3^{(1)} \right] \quad (38)$$

$$0 = \partial_{T_1} E_3 + \nabla_1 \cdot (c_{g,3} E_3) - \Re \left[ e^{i(\phi_2 + \phi_3 - \phi_1)/\epsilon^2} \frac{1}{2} \frac{N^2}{\hat{\omega}_3^2} (A_{312}^- + A_{321}^+) W_1^{(1)*} W_2^{(1)} W_3^{(1)} \right] \quad (39)$$

199 When summing the contributions of all members of the triad one gets

$$\begin{aligned} \partial_{T_1} (E) &= \partial_{T_1} (E_1 + E_2 + E_3) \\ &= - \left[ \nabla_1 \cdot (c_{g,1} E_1) + \nabla_1 \cdot (c_{g,2} E_2) + \nabla_1 \cdot (c_{g,3} E_3) \right] \\ &\quad - \Re \left[ i A e^{i(\phi_2 + \phi_3 - \phi_1)/\epsilon^2} W_1^{(1)*} W_2^{(1)} W_3^{(1)} \right] \end{aligned} \quad (40)$$

200 where  $A \in \mathbb{R}$  is equal to

$$A = -i \frac{1}{2} \left[ \frac{N^2}{\hat{\omega}_1^2} (A_{123}^+ + A_{132}^+) - \frac{N^2}{\hat{\omega}_2^2} (A_{213}^- + A_{231}^+) - \frac{N^2}{\hat{\omega}_3^2} (A_{312}^- + A_{321}^+) \right] \quad (41)$$

201 Here we note again that all wavenumbers and intrinsic frequencies depend on the slow time and spatial scales  
202 only. Thus in an  $\epsilon$ -neighborhood around exact resonance the resonance conditions (Eqs. 35 and 36) remain valid.

203 Applying these conditions to Eq. (41) yields

$$A = 0 \tag{42}$$

204 Thus the wave energy is conserved during the interaction of any triad. For any wave train  $\beta$  that is not a member of  
 205 a resonant triad the interaction terms vanish due to the asymptotic scale separation. Hence we have conservation of  
 206 the sum of the wave energies over all packets near resonance and write accordingly

$$0 = \sum_{\beta} [\partial_{T_1} E_{\beta} + \nabla_1 \cdot (c_{g,\beta} E_{\beta})] \tag{43}$$

#### 207 4.4 | Wave Impact During Interactions

208 While the evolution of  $U_0^{(1)}$  on the intermediate coordinates,  $(T_1, X_1)$ , is independent of the waves, it is influenced by  
 209 the gravity wave momentum flux convergences on the large-scale coordinates,  $(T_2, X_2)$  (not shown). However, since  
 210 the near-resonance solution is valid in an  $\epsilon$ -neighborhood in  $T_2$  around the exact resonance, the slow change of the  
 211 next-order mean flow is of the order  $O(\epsilon^2)$  with respect to the leading order. Also the term describing the impact of  
 212  $U_0^{(1)}$  on the wave fields in Eq. (31),  $i(U_0^{(1)} \cdot k_{\beta})W_{\beta}^{(1)}$ , may be interpreted as a next-order correction to the dispersion  
 213 relation. We therefore neglect the next-order horizontal mean flow,  $U_0^{(1)}$ .

214 Similarly, the leading-order vertical mean flow,  $W_0^{(4)}$ , is driven by gravity wave fluxes. Moreover it is related to  
 215 the leading-order buoyancy similar to the off-resonance solution. We thus conclude that the vertical mean flow is  
 216 generally dependent of the waves near resonance. However, we neglect this effect since there is no feedback on  
 217 the wave field and the largest non-zero vertical mean flow is three orders smaller compared to the assumed wave  
 218 amplitude.

## 219 4.5 | Matching the Solution Regimes

220 The prognostic and diagnostic equations for the regimes near and far from resonance were summarized above. Nat-  
 221 urally we require that in the limit,  $\epsilon \rightarrow 0$ , the mean flow and wave amplitudes of the same hierarchy must match at  
 222 the regime transition. To determine the regimes of validity of the solutions one may consider the validity of the phase  
 223 expansions. In particular, the near-resonance solution is valid in an  $\epsilon$ -neighborhood around the exact resonance on  
 224 the slow scales,  $(T_2, X_2) \in O(\epsilon)$ . Hence, we seek conditions so that the off-resonance solution matches the near-  
 225 resonant solution in the limit as the resonance manifold is approached. This corresponds to the limit  $(T_1, X_1) \rightarrow \pm\infty$   
 226 (cf. Glebov et al., 2005).

### 227 Mean Flow

228 The leading horizontal mean flow in both solutions are non divergent (Eqs. 12 and 23) and hydrostatic (Eqs. 13 and 28).  
 229 Moreover the leading-order buoyancy is independent of the wave field in the linear regime (Eq. 14). The evolution in  
 230 the near-resonance solution, averaged over  $(T_1, X_1)$ , is given by Eq. (30). Consequently the only matching condition  
 231 for the leading-order mean flow is given by

$$W_0^{(4)} \xrightarrow{(T_1, X_1) \rightarrow \pm\infty} \overline{W_0^{(4)}}^{(T_1, X_1)} \quad (44)$$

### 232 Wave Amplitudes

233 By assumption the wave properties, i.e.  $\omega_\beta$  and  $k_\beta$ , depend on the large-scale coordinates  $(T_2, X_2)$  and consequently  
 234 obey the eikonal equations (Eqs. 18 and 19) in both solutions. Moreover, the leading-order waves follow the dispersion  
 235 and polarization relations (Eqs. 15 and 16). While wave action is conserved off-resonance (Eq. 21), it is subject to  
 236 nonlinear exchange on the intermediate coordinates in the near-resonance solution (Eq. 33). To find the matching  
 237 conditions between the two solutions we thus seek the limit of the near-resonance solution for  $(T_1, X_1) \rightarrow \pm\infty$ . First

238 we note that the interaction term scales with exponential functions of phase differences

$$T_{\beta}^{(1)} \sim e^{\Delta\phi/\varepsilon^2} \quad (45)$$

239 By assumption one has  $-\partial_{T_2}\Delta\phi = \Delta\omega \sim O(1)$  and  $\nabla_2\Delta\phi = \Delta\mathbf{k} \sim O(1)$  in the limit  $(T_1, \mathbf{X}_1) \rightarrow \pm\infty$ . Thus the nonlinear  
240 forcing term can be expanded to leading order

$$e^{\Delta\phi/\varepsilon^2} \approx e^{i(\Delta\mathbf{k}\cdot\mathbf{X}_0 - \Delta\omega T_0)} \quad (46)$$

241 This term is dependent on the short-scale coordinates  $(T_0, \mathbf{X}_0)$ , and must therefore vanish after averaging over the  
242 large scales (cf. Danilov, 2001). Thus, in the limit  $(T_1, \mathbf{X}_1) \rightarrow \pm\infty$ , the wave action equation becomes a conservation  
243 law similar to the linear solution (Eq. 21).

$$0 = \partial_{T_1} \mathcal{A}_{\beta} + \nabla_1 \cdot (\mathbf{c}_{g,\beta} \mathcal{A}_{\beta}) \quad (47)$$

244 We conclude that in the limit  $(T_1, \mathbf{X}_1) \rightarrow \pm\infty$  the wave amplitudes are not driven by interaction on the intermediate  
245 scales. The formal matching condition is given by

$$\overline{\mathbf{V}_{\beta}^{(1)}}(T_1, \mathbf{X}_1) \xrightarrow{(T_1, \mathbf{X}_1) \rightarrow \pm\infty} \mathbf{V}_{\beta}^{(1)} \quad (48)$$

## 246 5 | SUMMARY OF DIMENSIONAL EQUATIONS IN 1.5D

247 For the application of the above-derived equations we revert to dimensional variables. Moreover we assume homo-  
 248 geneity of mean flow and wave amplitudes in the horizontal direction such that the equations become effectively  
 249 one dimensional (cf. Muraschko et al., 2015). Finally we also assume that the horizontal mean-flow velocity,  $U_0^{(0)}$ , as  
 250 well as the horizontal wave vectors,  $k_{\beta}$ , have an  $x$ -component only. Under these assumptions the incompressible,  
 251 constant, and hydrostatic mean flow satisfies in both regimes

$$0 = w_0 \qquad \qquad \qquad 0 = \partial_x u_0 \qquad \qquad \qquad (49)$$

$$0 = \partial_t u_0 \qquad \qquad \qquad 0 = \partial_z p_0 - b_0 \qquad \qquad \qquad (50)$$

252 The waves are governed by the eikonal equations (Eqs. 18 and 19), the dispersion and polarization relations (Eqs. 15  
 253 and 16), and the wave action or wave amplitude equations (Eqs. 21, 31, and 33). The dimensional eikonal equations  
 254 are

$$(\partial_t + c_{g,z,\beta} \partial_z) \omega_\beta = 0 \qquad \qquad \qquad (51)$$

$$(\partial_t + c_{g,z,\beta} \partial_z) k_\beta = -e_z k_\beta \partial_z u_0 \qquad \qquad \qquad (52)$$

255 with the dispersion relation

$$\hat{\omega}_\beta^2 = \frac{N^2 k_\beta^2}{k_\beta^2 + m_\beta^2} \qquad \qquad \qquad (53)$$

256 and the group velocities

$$\hat{c}_{g,\beta} = \frac{\hat{\omega}_\beta^3}{N^2} \frac{m_\beta}{k_\beta^2} \left( \frac{k_\beta m_\beta}{k_\beta^2}, 0, -1 \right)^T = c_{g,\beta} - u_0 \quad (54)$$

257 The polarization relations are

$$\mathbf{Z}_\beta = \left( u_\beta, v_\beta, w_\beta, \frac{b_\beta}{N}, p_\beta \right)^T = w_\beta \left( -\frac{m_\beta}{k_\beta}, 0, 1, \frac{N}{i\hat{\omega}_\beta}, -\frac{m_\beta \hat{\omega}_\beta}{k_\beta^2} \right)^T \quad (55)$$

258 While wave action conservation holds for the linear off-resonant solution, i.e.

$$0 = \partial_t \mathcal{A}_\beta + \partial_z (c_{g,z,\beta} \mathcal{A}_\beta) \quad (56)$$

259 the near-resonance regime requires additional interaction terms such that

$$\begin{aligned} 0 = & \partial_t \mathcal{A}_\beta + \partial_z (c_{g,z,\beta} \mathcal{A}_\beta) \\ & + \frac{1}{2} \frac{N^2}{\hat{\omega}_\beta^3} \Re \left[ \sum_{\gamma,\delta} e^{i(\varphi_\gamma + \varphi_\delta - \varphi_\beta)} A_{\beta\gamma\delta}^+ w_\beta^* w_\gamma w_\delta + \sum_{\gamma,\delta} e^{i(-\varphi_\gamma - \varphi_\delta - \varphi_\beta)} A_{\beta\gamma\delta}^- w_\beta w_\gamma^* w_\delta^* \right. \\ & \left. + \sum_{\gamma \neq \delta} e^{i(\varphi_\gamma - \varphi_\delta - \varphi_\beta)} A_{\beta\gamma\delta}^- w_\beta^* w_\gamma w_\delta^* + \sum_{\gamma \neq \delta} e^{i(-\varphi_\gamma + \varphi_\delta - \varphi_\beta)} A_{\beta\gamma\delta}^+ w_\beta w_\gamma^* w_\delta^* \right] \quad (57) \end{aligned}$$

260 where the interaction coefficients are given by

$$A_{\beta\gamma\delta}^{\pm} = \pm i \frac{1}{4} \frac{\hat{\omega}_{\beta}^2}{N^2} \left( m_{\delta} - m_{\gamma} \frac{k_{\delta}}{k_{\gamma}} \right) \left[ \frac{m_{\beta} m_{\delta}}{k_{\beta} k_{\delta}} + 1 \pm \frac{N^2}{\hat{\omega}_{\delta} \hat{\omega}_{\beta}} \right] \quad (58)$$

261 Equation (57) is, however, ill posed when the wave amplitude,  $w_{\beta}$ , is zero at an initial time. Instead we solve the

262 complex wave amplitude equation given by

$$\begin{aligned} 0 = & (\partial_t + c_{g,z,\beta} \partial_z) w_{\beta} \\ & + \sum_{\gamma,\delta} e^{i(\varphi_{\gamma} + \varphi_{\delta} - \varphi_{\beta})} A_{\beta\gamma\delta}^{+} w_{\gamma} w_{\delta} + \sum_{\gamma,\delta} e^{i(-\varphi_{\gamma} - \varphi_{\delta} - \varphi_{\beta})} A_{\beta\gamma\delta}^{-} w_{\gamma}^{*} w_{\delta}^{*} \\ & + \sum_{\gamma \neq \delta} e^{i(\varphi_{\gamma} - \varphi_{\delta} - \varphi_{\beta})} A_{\beta\gamma\delta}^{-} w_{\gamma} w_{\delta}^{*} + \sum_{\gamma \neq \delta} e^{i(-\varphi_{\gamma} + \varphi_{\delta} - \varphi_{\beta})} A_{\beta\gamma\delta}^{+} w_{\gamma}^{*} w_{\delta} \end{aligned} \quad (59)$$

263 where the second-order horizontal mean flow is neglected. The evolution of the phase functions,  $\phi_{\beta}$ , along the wave

264 characteristics is given by the definition of the wavenumber and frequency

$$(\partial_t + c_{g,z,\beta} \partial_z) \varphi_{\beta} = (-\omega_{\beta} + c_{g,z,\beta} m_{\beta}) \quad (60)$$

265 where we have rescaled the phase function such that  $\varphi_{\beta} = \epsilon^{-2} \phi_{\beta}$ . Hence the small parameter  $\epsilon$  does not appear

266 explicitly in the equations.

267 Eqs. (51), (52), and (56) are equivalent to Grimshaw's modulation equations (Grimshaw, 1977, 1988) for weakly

268 nonlinear non-hydrostatic internal gravity waves. Here, Eq. (57) replaces Eq. (56) where near resonant triad inter-

269 actions are relevant and the nonlinearities come into play. This system may be employed numerically to estimate

270 wave-wave interactions in the context of WKBJ ray-tracing simulations as discussed below.

## 271 6 | A SEMI-EMPIRICAL PARAMETERIZATION FOR THE INTERACTION EQUA- 272 TIONS

273 In the previous sections we have presented a weakly nonlinear multi-wave WKBJ theory based on the non-hydrostatic  
274 Boussinesq equations. The resulting modulation equations are summarized in Eqs. (49) to (59) assuming horizontal  
275 homogeneity so that they are effectively one-dimensional. These equations may be solved numerically using several  
276 approaches.

### 277 **Phase expansion around resonance**

278 Following Grimshaw (1988), near the manifold of exact resonance, one may expand the phase functions,  $\phi_\beta$ , to second  
279 order in time and space and project the resulting interaction equations onto a space-time direction which is perpen-  
280 dicular to the resonance manifold in  $z$ - $t$ -space. In the limit  $\epsilon \rightarrow 0$  the exchange of energy among the members of a  
281 triad implied by the near-resonance solution then appears as a “jump” across the resonance manifold. However, in  
282 implementing this approach we encountered certain difficulties. In particular the projection onto the cross-resonance  
283 coordinate leads to singularities and secular growth in the interaction equations where the space-time trajectory of  
284 any triad member is parallel to the resonance manifold. Also, singularities may occur where the second order trunca-  
285 tion of the phase expansion becomes invalid and the equations have to be rescaled. Since both these issues do arise  
286 at rather common settings of wavenumbers and background shear strengths, we do not follow this approach.

### 287 **Equivalent window method**

288 We observe that the exponential term in the interaction equations (Eq. 59) acts as an integration window limiting the  
289 interaction, depending on the spectral deviation from resonance. We thus suggest to find a spectral window function  
290 with an equivalent width. In such a case the interaction equations may be solved as if in exact resonance but limited



291 in terms of spectral deviation from resonance. This approach is explained below.

292 The asymptotic theory presented earlier comprises two scaling regimes. While the off-resonance solution follows  
 293 linear dynamics on slow time and spatial scales, with corresponding coordinates,  $(T_2, \mathbf{X}_2)$ , the near-resonance solution  
 294 is characterized by the interaction of GW triads on intermediate time and spatial scales, with a dependence on  $(T_1, \mathbf{X}_1)$ .  
 295 In both cases the background is assumed to vary on the slow scales only. Thus near resonance and in the asymptotic  
 296 limit  $\epsilon \rightarrow 0$  the characteristic length scales of both the wave train amplitudes and the background shear are virtually  
 297 infinite with respect to the interaction (i.e. intermediate) scales. Motivated by this asymptotic limit we consider gravity  
 298 waves in a constant background shear  $\partial_z u_0 \neq 0$  with infinite extent in the vertical. Similarly, the slowly varying  
 299 wavenumbers,  $m_\beta$ , are assumed to be homogeneous in the vertical such that

$$\partial_z m_\beta = 0 \tag{61}$$

300 Consequently, the local tendency of the wave frequencies can be expressed as

$$\begin{aligned} \partial_t \omega_\beta &= -c_{g,z,\beta} \partial_z \omega_\beta \\ &= -c_{g,z,\beta} (c_{g,z,\beta} \partial_z m_\beta + k_\beta \partial_z u_0) \\ &= -k_\beta c_{g,z,\beta} \partial_z u_0 \end{aligned} \tag{62}$$

301 where we have used the eikonal equations (Eqs. 51 and 52), the fact that the wave frequencies and wavenumbers  
 302 are related by  $-\partial_z \omega_\beta = \partial_z \partial_t \varphi_\beta = \partial_t m_\beta$ , as well as the above assumption  $\partial_z m_\beta = 0$ . Expanding the phase difference

303 locally in time one finds

$$\Delta\varphi = (\Delta\varphi)_0 - (\Delta\omega)_0(t - t_0) - \frac{1}{2}(\partial_t\Delta\omega)_0(t - t_0)^2 \quad (63)$$

304 where the linear term vanishes when expanding around exact resonance. Moreover in resonance one has  $(\Delta k)_0 = 0$ .

305 Also, without loss of generality we set  $(\Delta\phi)_0 \equiv 0$ . Finally the phase difference becomes approximately

$$\Delta\varphi = -\frac{1}{2}(\partial_t\Delta\omega)_0(t - t_0)^2 = -\frac{1}{2}(\partial_t\Delta\hat{\omega})_0(t - t_0)^2 \quad (64)$$

306 For an explicit triad the interaction equations (Eq. 59) thus are

$$(\partial_t + c_{g,z,1}\partial_z)w_1 = A_1w_2w_3e^{i\Delta\varphi} \quad (65)$$

$$(\partial_t + c_{g,z,2}\partial_z)w_2 = A_2w_1w_3^*e^{-i\Delta\varphi} \quad (66)$$

$$(\partial_t + c_{g,z,3}\partial_z)w_3 = A_3w_1w_2^*e^{-i\Delta\varphi} \quad (67)$$

307 where the phase difference is  $\Delta\varphi = \varphi_2 + \varphi_3 - \varphi_1$  and the interaction coefficients are given by

$$A_1 = -(A_{123}^+ + A_{132}^+) \quad (68)$$

$$A_2 = -(A_{213}^- + A_{231}^+) \quad (69)$$

$$A_3 = -(A_{312}^- + A_{321}^+) \quad (70)$$

308 Inserting the local phase evolution (Eq. 64) one finds that the right hand sides in Eqs. (65) to (67) are independent of the  
 309 vertical coordinate,  $z$ . Thus the homogeneity assumption can be repeated for the wave amplitudes,  $w_\beta$ . Consequently  
 310 the vertical gradients vanish at any time and height,  $\partial_z w_\beta \equiv 0$ . Hence the system Eqs. (65) to (67) simplifies to

$$\partial_t w_1 = A_1 w_2 w_3 e^{-i \frac{1}{2} (\partial_t \Delta \hat{\omega})_0 (t-t_0)^2} \quad (71)$$

$$\partial_t w_2 = A_2 w_1 w_3^* e^{i \frac{1}{2} (\partial_t \Delta \hat{\omega})_0 (t-t_0)^2} \quad (72)$$

$$\partial_t w_3 = A_3 w_1 w_2^* e^{i \frac{1}{2} (\partial_t \Delta \hat{\omega})_0 (t-t_0)^2} \quad (73)$$

311 where the dephasing,  $\frac{1}{2} (\partial_t \Delta \hat{\omega})_0$ , can be expressed in terms of the wavenumbers using Eq. (62)

$$(\partial_t \Delta \hat{\omega})_0 = -(k_2 c_{g,z,2} + k_3 c_{g,z,3} - k_1 c_{g,z,1})_0 \partial_z u_0 \quad (74)$$

312 This system of equations is equivalent to the evolution of plane waves in a background shear flow with infinite extent.

313 This image may be useful to understand the asymptotic, i.e. local, passage through resonance.

314 For comparison, we set up a simplified system making use of the fact that in a small neighborhood around exact  
 315 resonance the resonance conditions are satisfied approximately. To balance the limited width of validity of approxi-  
 316 mately exact resonance one may introduce a window function  $G(t - t_0)$  of the form

$$G(t - t_0) = \theta(t^\dagger - |t - t_0|) \quad (75)$$

317 where  $\theta$  represents the Heaviside function. This represents a symmetric box with value  $G = 1$  around the resonance

318 time  $t_0$ , and value  $G = 0$  elsewhere. A simplified system then reads

$$\partial_t w_1 = A_1 w_2 w_3 G(t - t_0) \quad (76)$$

$$\partial_t w_2 = A_2 w_1 w_3^* G(t - t_0) \quad (77)$$

$$\partial_t w_3 = A_3 w_1 w_2^* G(t - t_0) \quad (78)$$

319 To evaluate  $G(t - t_0)$  one may compare Eqs. (76) to (78) to Eqs. (71) to (73) with a quadratic dephasing near resonance  
 320 as described above. Integrating the exponential term over the time corresponding to a local asymptotic expansion,  
 321 i.e. from  $-\infty$  to  $\infty$ , yields the Fresnel integral

$$I_F = \int_{-\infty}^{\infty} e^{i \frac{1}{2} (\partial_t \Delta \hat{\omega})_0 (t - t_0)^2} dt = \sqrt{\frac{i 2\pi}{(\partial_t \Delta \hat{\omega})_0}} \quad (79)$$

322 Equating the absolute value of the real part of  $I_F$  with the integral over the window,  $G(t - t_0)$ , yields

$$I_G = \int_{t_0 - t^\dagger}^{t_0 + t^\dagger} dt = 2t^\dagger = \sqrt{\frac{2\pi}{|(\partial_t \Delta \omega)_0|}} = |I_F| \quad (80)$$

323 giving a first-order estimate for the window half width,  $t^\dagger$ . In order to practically apply this estimate one would,  
 324 however, need to solve for the exact resonance manifold and consecutively reconstruct the effective interaction region  
 325 before integrating the model. We therefore evaluate  $t^\dagger$  in terms of an effective spectral resonance deviation which  
 326 can be readily diagnosed during run time of the model integration. In particular we define a normalized resonance

327 function  $R$  such that

$$R(t) = \frac{\hat{\omega}_2 + \hat{\omega}_3 - \hat{\omega}_1}{\hat{\omega}_2 + \hat{\omega}_3} = \frac{\Delta\hat{\omega}}{\hat{\omega}_2 + \hat{\omega}_3} = \frac{(\partial_t \Delta\hat{\omega})_0}{\hat{\omega}_2 + \hat{\omega}_3} (t - t_0) \quad (81)$$

328 Thus the resonance function at the boundaries of the interaction window  $G(t - t_0)$  is given by

$$|R(t_0 + t^\dagger)| = |R(t_0 - t^\dagger)| = \frac{\sqrt{2\pi} |(\partial_t \Delta\hat{\omega})_0|}{2(\hat{\omega}_2 + \hat{\omega}_3)} = \frac{\sqrt{2\pi} |(k_2 c_{g,z,2} + k_3 c_{g,z,3} - k_1 c_{g,z,1}) \partial_z u_0|}{2(\hat{\omega}_2 + \hat{\omega}_3)} \quad (82)$$

329 Equation (82) directly gives a leading-order estimate for the spectral resonance width. This estimate covers the  
 330 dependencies on the wavenumbers and background shear but may need tuning for a global parameterization. We  
 331 therefore introduce a tuning parameter,  $\kappa$ , and set the spectral window

$$G(t) = \tilde{G}(R(t)) = \theta(R^\dagger - |R(t)|) \quad (83)$$

332 where  $\theta$  denotes the Heaviside step function and  $R^\dagger = \kappa |R(t_0 \pm t^\dagger)|$ . The parameter  $\kappa$  may then be optimized for  
 333 best agreement between simulation results of Eqs. (71) to (73) and Eqs. (76) to (78). This formulation now allows for  
 334 simulations that locally diagnose resonance deviations and enable interactions where necessary without solving for  
 335 exact resonance manifolds.

336 Note that the described procedure approximates the interaction equations Eqs. (65) to (67) such that the total  
 337 changes of the magnitude of the complex wave amplitudes,  $w_\beta$ , are recovered. However, the parametrization intro-  
 338 duces a modification of the phases of the complex wave amplitudes which are then bound to differ from the full  
 339 solution. Analyzing interaction systems with constant phase difference Bustamante and Kartashova (2009) find that

340 this may modify the evolution of the wave amplitudes in terms of both energy exchange rates and maximum energy  
 341 exchange. While the effective resonance interval,  $R^\dagger$ , is chosen such that the total energy exchange is recovered  
 342 deviations in the exact evolution between the full and the parametrized solution may occur.

## 343 6.1 | Estimating the Tuning Parameter $\kappa$

344 In order to estimate the tuning parameter,  $\kappa$ , we compare numerical results of the reference system given by Eqs. (71)  
 345 to (73) and the system Eqs. (76) to (78) with Eq. (83) for a range of specific resonances. With a length scale  $\tilde{L} = 5 \text{ km}/2\pi$   
 346 we consider triads with non-dimensional horizontal wavenumbers  $\hat{k}_1 = 0.2$  and  $\hat{k}_2 = \hat{k}_3 = 0.1$ . While  $\hat{m}_1$  and  $\hat{m}_3$  follow  
 347 from the resonance conditions  $\hat{m}_2 + \hat{m}_3 - \hat{m}_1 = 0$  and  $\hat{\omega}_2 + \hat{\omega}_3 - \hat{\omega}_1 = 0$ , the non-dimensional vertical wavenumber  
 348 of the second GW is chosen from the interval  $\hat{m}_2 \in [0.56, 10]$ . Here the lower boundary corresponds to the lowest  
 349 wavenumber at which Eqs. (71) to (73) can be solved while avoiding passage through a second distinct resonance. The  
 350 upper boundary is chosen in accordance with the asymptotic assumption  $\hat{m}_2 = \mathcal{O}(1)$ . We thus consider dimensionful  
 351 horizontal wavelengths of the order  $\sim 10 \text{ km}$  and vertical wavelengths of the order  $\sim 1 \text{ km}$ . In general atmospheric  
 352 GWs cover a broad range of spatial scales (Callies et al., 2014). Here we choose rather small wavelengths for GWs in  
 353 order to be consistent with the simplification of non-rotating Boussinesq dynamics. A critical reader will notice that  
 354 most of the cases considered imply  $|m_\beta/k_\beta| \gg 1$ , not quite consistent with the original non-dimensionalization of the  
 355 Boussinesq equations, where equal horizontal and vertical length scales have been assumed. This is, however, only  
 356 an apparent violation of the assumptions. Redoing the scale-asymptotic analysis with anisotropic scaling leads to a  
 357 limiting form of the presented formulae with  $k_\beta^2 \ll m_\beta^2$  in Eqs. (53) and (58). All other results stay intact. However,  
 358 while our formulation is quite general we present results for relatively anisotropic test cases so that the interaction  
 359 coefficients (Eq. 58) are larger and strong energy exchanges may be observed.

360 As for wave and shear amplitudes, in accordance with the weakly nonlinear theory, the initial amplitude of the  
 361 wave trains relative to the corresponding static instability criterion are varied between  $10^{-3}$  and  $10^{-1}$ . The chosen  
 362 background shear strength is equal to a value corresponding to the maximum shear in our reference simulations  
 363 which are introduced in the later part of this study. In particular  $\partial_z u = 2\pi/40,000 \text{ s}^{-1} \approx 1.6 \times 10^{-4} \text{ s}^{-1}$ . This value

364 corresponds to relatively weak sheared background winds in the atmosphere where jet strengths  $U = O(10 \text{ m s}^{-1})$   
 365 and a tropopause height  $H = O(10 \text{ km})$  imply  $\partial_z u = O(10^{-3} \text{ s}^{-1})$ . However, as shown in the discussion, there are large  
 366 areas, for instance in the mid-latitudes and polar regions in spring and autumn after the break down of the polar night  
 367 jet, that are well represented by a shear strength  $\partial_z u = O(10^{-4} \text{ s}^{-1})$ . Moreover, it allows for a strong wave modulation  
 368 (order  $O(1)$ ) on time scales approximately two orders of magnitude longer than a typical wave period ( $\sim 10^3 \text{ s}$ ). The  
 369 chosen background shear is therefore consistent with both the scaling assumptions of the asymptotic theory as well  
 370 as observed atmospheric conditions. Stronger shears will be discussed below as well, and it will be shown there that  
 371 the associated wave modulation by the mean flow partially suppresses the non-linear interactions.

372 Optimal values for the parameter  $\kappa$  are then found for 189 central wavenumbers  $m_2$  and 21 different amplitudes  
 373 within the given intervals. In particular we use a Nelder-Mead procedure to find the least square deviation between  
 374 the the two model results (Nelder and Mead, 1965). We find that the optimal value for  $\kappa$  is approximately constant  
 375 for all central wavenumbers and in the limit of small amplitudes (Fig. 1). For amplitudes near  $10^{-1}$  the optimal tuning  
 376 parameter decreases with minimum values as low as 0.04. In this regime the characteristic time scales of the exactly  
 377 resonant system are comparable to the time scales given by the dephasing (cf. Eq. 74). This causes a potential sys-  
 378 tematic bias to this method at large amplitudes. The median of all optimal values for 189x21 evaluations, spanning the  
 379 intervals  $\hat{m}_2 \in [0.56, 10]$  and  $\alpha \in [10^{-3}, 10^{-1}]$ , is equal to  $\kappa = 0.9969 \approx 1$ .

380 The approximately constant  $\kappa$  shows that the form of the effective spectral interaction threshold,  $R^\dagger$  (Eq. 82),  
 381 covers the dependency on the wavenumbers with high accuracy. This strongly suggests that a globally constant  $\kappa$   
 382 may describe the spectral interaction threshold across a wide range of wavenumber scales. Moreover the constant  
 383 optimal tuning parameter,  $\kappa \approx 1$ , for small amplitudes suggests that the derived effective spectral interaction threshold,  
 384  $R^\dagger$ , in combination with a global tuning parameter,  $\kappa$ , are appropriate to parameterize the spectral passage through a  
 385 resonance across all scales covered by the asymptotic theory. However, for amplitudes approaching the limit of static  
 386 instability at  $O(1)$  the parameterization, understandably, may not be as accurate.

387 For a qualitative error estimate we visualize the difference between numerical solutions to the simplified system  
 388 (Eqs. 71 to 73) and the parametrized system (Eqs. 76 to 78) in Fig. 2. Here we distinguish wave amplitudes solving  
 389 the simplified system,  $w_j^{(s)}$ , and wave amplitudes solving the parameterized system,  $w_j^{(p)}$ . The parameters for the

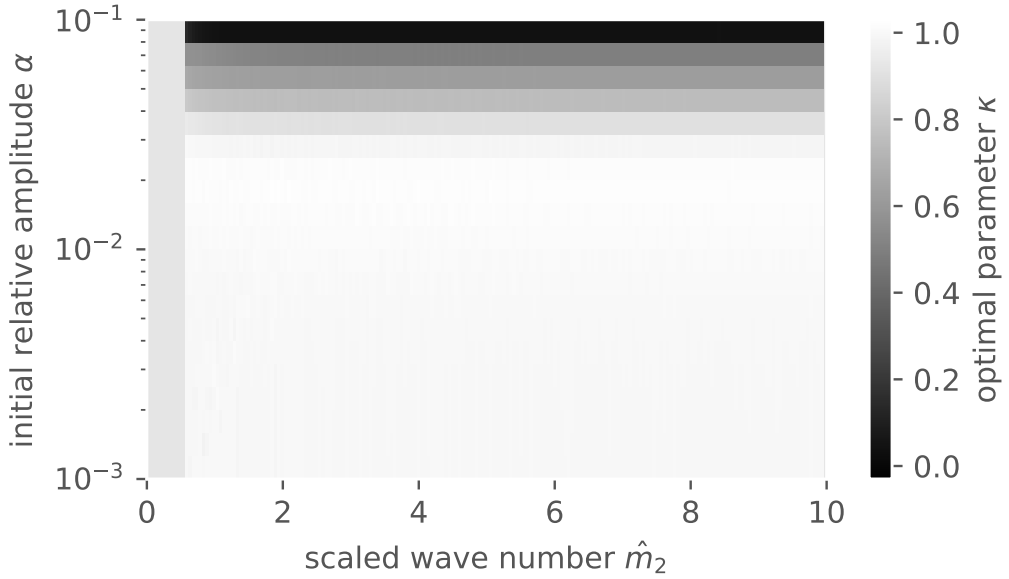


**FIGURE 1** Optimal tuning parameter  $\kappa$  dependent on the central resonance triad and wave amplitudes. The median has a value of  $\kappa = 0.9969 \approx 1$ .

390 shown simulation are  $\partial_z u = 2\pi/40,000 \text{ s}^{-1}$ ,  $\hat{k}_1 = 0.2$ ,  $\hat{k}_2 = \hat{k}_3 = 0.1$ ,  $\hat{m}_2 = 5$ ,  $\kappa = 1$ , and  $\alpha = 10^{-2}$ . Considering  
 391 the trajectories of the solutions on the complex plane (cf. Fig. 2a - c) it is evident that the parametrized solution (blue)  
 392 cannot reproduce the evolution of the phases of the complex wave amplitudes of the simplified solution (red). Despite  
 393 this obvious shortcoming the parametrization predicts the total change of the absolute value of the wave amplitudes  
 394 with small errors (cf. Fig. 2d - f).

395 To highlight the quantitative error we compute solutions to both systems for the previously used parameter  
 396 space and evaluate the ratios of the resulting energies after the interaction. In particular we choose relative wave  
 397 amplitudes  $\alpha \in [10^{-3}, 10^{-1}]$ , central wavenumbers  $\hat{m}_2 \in [0.56, 10]$ , a background shear  $\partial_z u = 2\pi/40,000 \text{ s}^{-1}$ , and  
 398 a parametrization constant  $\kappa \equiv 1$ . As a diagnostic we calculate the ratio of the wave energies of the two solutions  
 399 after the interaction for each triad member,  $E_j^{(p)}/E_j^{(s)} = |w_j^{(p)}|^2 / |w_j^{(s)}|^2$ . We find that the deviation is generally  
 400 smaller than 8% with a mean and median value  $< 2\%$  for all three triad members over the whole tested parameter  
 401 space (Fig. 3). Systematic biases arise at initial relative amplitudes  $\alpha > 0.04$ . Here the energy transferred to the



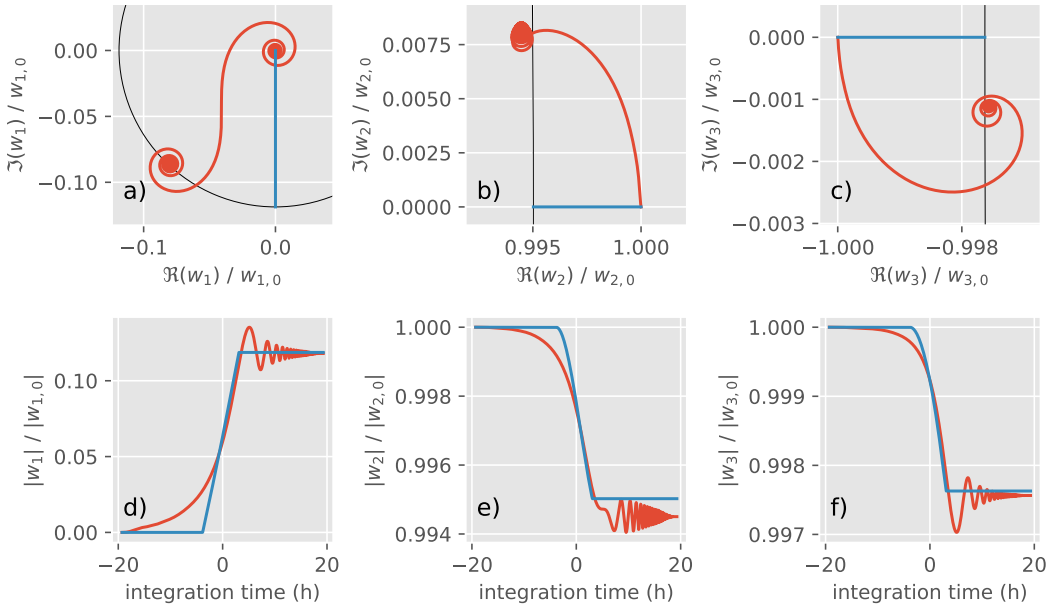


**FIGURE 2** Example solutions to the simplified system (Eqs. 71 to 73, depicted in red) and the parametrized system (Eqs. 76 to 78, shown in blue) for  $\partial_z u = 2\pi/40,000 \text{ s}^{-1}$ ,  $k_1 = 0.2$ ,  $k_2 = k_3 = 0.1$ ,  $\hat{m}_2 = 5$ ,  $\kappa = 1$ , and  $\alpha = 10^{-2}$ . The panels (a) through (c) show the trajectories of the solutions on the complex plane. Black arcs represent the level of constant magnitude corresponding to the parametrized amplitude,  $w_j^{(p)}$ , after the interaction. Panels (d) through (f) show the time evolution of the absolute value of the amplitudes,  $w_j^{(p)}$  and  $w_j^{(s)}$ , relative to their initial value. Each column corresponds to one of the three triad members.

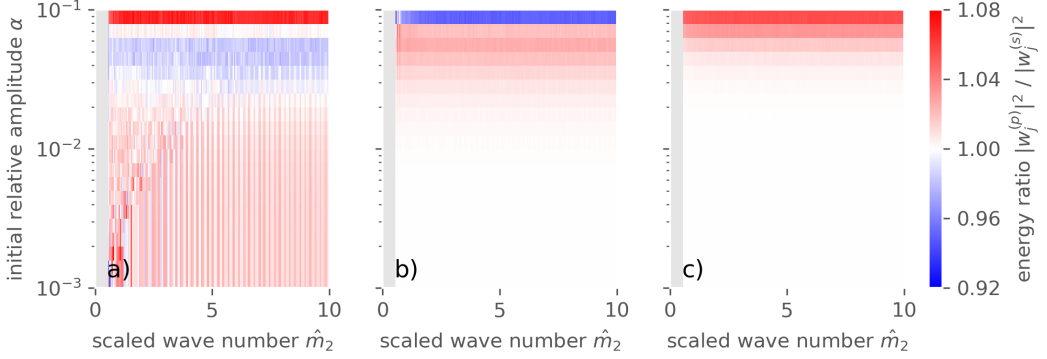


**FIGURE 3** Ratios of wave energies corresponding of the solutions the simplified system (Eqs. 71 to 73) and the parametrized system (76 to 78) after the interaction. Here, the background shear is set to  $\partial_z u = 2\pi/40,000 \text{ s}^{-1}$ , and the parametrization constant is  $\kappa \equiv 1$ . Panel (a), (b), and (c) are associated to  $j = 1$ ,  $j = 2$ , and  $j = 3$ , correspondingly.

402 generated triad member may be either under- or overestimated (Fig. 3a). Strongest deviations occur near  $\alpha = 0.1$   
 403 where the parametrization leads to overestimates of the transferred energy while overestimating and underestimating  
 404 the energy of either one of the generating triad members (Fig. 3a-c).

## 405 7 | VERIFICATION WITH IDEALIZED TEST CASES

### 406 7.1 | The Test Case Definition

407 As a generic test case we use the generation of a third wave train through the resonant interaction of two given  
 408 wave trains. A predefined sinusoidal background shear modulates the given wave trains to enable spectral passage  
 409 through resonance. In particular we use a periodic domain of height  $H = 40 \text{ km}$  (so that  $H/\bar{L} = 16\pi$ ) and a background  
 410 shear flow defined as  $u = u_0 \sin(2\pi z/H)$ . In the tests below,  $u_0 \in [0, 1 \text{ m s}^{-1}]$ . The maximum shear is therefore  
 411 approximately  $\partial_z u_0 \approx 1.6 \times 10^{-4} \text{ s}^{-1}$ . Based on this mean-flow profile we derive initial conditions for the wave trains  
 412 such that the modulated wave-wave interaction takes place near the center of the domain. Note that the vertical scale  
 413  $H$  is much larger than the considered vertical wavelengths. Thus this structure of the mean-flow is compliant with  
 414 both the periodic boundary conditions of the simulations and the slow modulation assumption. As initial conditions

415 for the given wave trains we consider Gaussian wave packets with vertical velocities

$$w_j = w_{j,0} e^{-\frac{(z-z_j)^2}{2\sigma^2}} \cos(m_j z) \quad (84)$$

416 The center of the wave trains,  $z_j$ , and initial wavenumbers,  $m_j$ , are chosen such that the wave trains are in resonance  
 417 and overlap in the center of the domain after approximately half the integration time, as described below. The latter  
 418 is chosen such that at the final time the energy exchange is negligible. The initial wave amplitudes are taken to be a  
 419 given fraction,  $\alpha$ , with respect to the static instability criterion (e.g. Achatz et al., 2017). In particular

$$w_{j,0} = \alpha \frac{\omega(k_j, m_j)}{m_j} \quad (85)$$

420 All other initial fields are determined through the polarization relations (Eq. 55). Wave amplitudes considered below  
 421 are in the range  $\alpha \in [10^{-2}, 10^{-0.4}]$ . The initial packet width is constant with  $\sigma = 2$  km, the horizontal wavelengths  
 422 are set to  $\lambda_2 = \lambda_3 = 50$  km such that  $\lambda_1 = 25$  km. These wavelengths correspond to non-dimensional wavenumbers  
 423  $\hat{k}_1 = 0.2$  and  $\hat{k}_2 = \hat{k}_3 = 0.1$ . They are chosen such that the interaction coefficients (Eq. 32) are large enough for the  
 424 resonance conditions to permit a wide range of wavenumbers  $\hat{m}_2$  for exact resonances. Validations against cases with  
 425 larger horizontal wavenumbers have been done as well (not shown), with qualitatively similar results to those reported  
 426 here.

## 427 7.2 | WKBJ validation against wave resolving simulations

428 For qualitative and quantitative comparisons we run wave-resolving simulations as well as WKBJ ray-tracing simula-  
 429 tions with equivalent initial conditions. In particular we employ, in Boussinesq mode, the code PincFloit with a second-

430 order MUSCL scheme utilizing an MC flux limiter (Rieper et al., 2013b; Wilhelm et al., 2018). The time integration is  
 431 realized through a third-order Runge-Kutta scheme. To circumvent numerical attenuation, it is run with a resolution  
 432 that permits for at least 12 points per wavelength in the initial conditions. For comparison we use the spectral WKB  
 433 ray-tracing code introduced by Muraschko et al. (2015), augmented by an interaction module corresponding to the  
 434 parameterized solution method presented in Section 6. A brief technical description of the implementation can be  
 435 found in the appendix. The wave-resolving simulations are carried out in two dimensions with a periodic horizontal  
 436 domain. In particular we set the domain such that it has a horizontal extent equal to a multiple of the horizontal  
 437 wavelengths of the wave, and we employ periodic boundary conditions.

438 We choose three distinct resonances with different resonant wavenumber triads around which we construct  
 439 the simulation. In particular the central triads are characterized by the non-dimensional vertical wavenumbers,  $\hat{m}_\beta$ ,  
 440 as summarized in Table 2. To define appropriate initial conditions for the test cases, the ray tracer was employed  
 441 with the interaction scheme disabled and using a negative time step, thus integrating backward in time. The initial  
 442 conditions were chosen to be Gaussian wave packets in exact resonance, the reverse integration time was set to  
 443 half the desired model integration time for the corresponding test case. The maximum amplitude position and mean  
 444 wavenumber of the resulting wave trains were used to set  $z_\beta$  and  $m_\beta$  in the initial conditions for the test cases (cf. Eq.  
 445 84). The initial amplitudes are set to  $\alpha = 0.1$  where the background shear is varied and the background velocity is set  
 446 to  $u_0 = 1 \text{ m s}^{-1}$  where the amplitudes are varied. In general the amplitudes do not only vary during triadic interactions  
 447 but also elsewhere due to the wave modulation and the wave action conservation (Eqs. 21 and 22). Thus the initial  
 448 amplitudes are not equivalent to the amplitude at the transition to the near-resonance regime. However, in cases of  
 449 small background velocities,  $u_0 \leq 1 \text{ m s}^{-1}$ , the effect is small and the initial amplitude remains a good estimate as to  
 450 how strong the waves are relative to static instability near resonance. For stronger background velocities, where the  
 451 modulation effect dominates the experiments, the amplitude modulation influences the strength of the interactions.  
 452 It is therefore balanced by modifying the initial amplitude such that the amplitude are comparable in the interaction  
 453 regime.

454 For the analysis and visualization the fields from the wave-resolving simulations are first Fourier-transformed in  
 455 both spatial directions, then separated by wavenumber and projected onto the polarization relations (Eq. 55). After

**TABLE 2** Resonant vertical wavenumber triads used for the simulations. The corresponding horizontal wavenumbers are  $(\hat{k}_1, \hat{k}_2, \hat{k}_3) = (0.2, 0.1, 0.1)$ . By convention the first wavenumber corresponds to the generated wave train such that  $\hat{k}_1 = \hat{k}_2 + \hat{k}_3$  and  $\hat{m}_1 = \hat{m}_2 + \hat{m}_3$ .

$\hat{m}_1$	$\hat{m}_2$	$\hat{m}_3$
2.93	5	-2.07
5.86	10	-4.14
8.79	15	-6.21

456 this filtering of each of the three contributing waves, the corresponding fields are used to determine the wave energy  
 457 densities of the individual wave trains in physical space. This procedure is similar to the one used by Borchert et al.  
 458 (2014), however without a separate local Fourier transform around each grid cell. To estimate energy exchanges the  
 459 energy densities were integrated in the vertical and compared among the individual triad members. For convenience  
 460 we normalize the vertically integrated wave energy densities by the sum of all triad components.

### 461 7.3 | Energetics of the Interacting Wave Trains

462 An example of the total wave energy density corresponding to the case with  $\hat{m}_2 = 10$  and  $u_0 = 1 \text{ m s}^{-1}$  is shown in  
 463 Fig. 4. Note that the energy of the background flow is filtered and not shown due to the projection onto the wave  
 464 modes. Naturally, the WKBJ simulations do not account for the variation on the scale of the wave lengths and lack  
 465 structure with respect to the wave-resolving simulations (Fig. 4b). As a result interference patterns with high wave  
 466 energy densities are not present in the WKBJ simulations. However, the evolution of the wave train amplitudes are  
 467 reproduced both qualitatively and quantitatively.

468 Separating the fields into the distinct wave trains and integrating the wave energy densities in the vertical as  
 469 explained above we find a generally good agreement in the temporal evolution of the individual wave energy densities  
 470 (Fig. 5). For early times,  $t \leq 24 \text{ h}$ , and late times,  $t \geq 48 \text{ h}$ , there is approximately no wave-wave interaction and  
 471 the evolution of the wave trains is dominated by the wave modulation through the background shear flow (Fig. 5a).  
 472 Naturally the weakly non-linear multi-scale WKBJ theory is an approximation to the fully non-linear dynamics. As an  
 473 example the waves in the wave-resolving simulations may be modulated not only due to the prescribed mean-flow

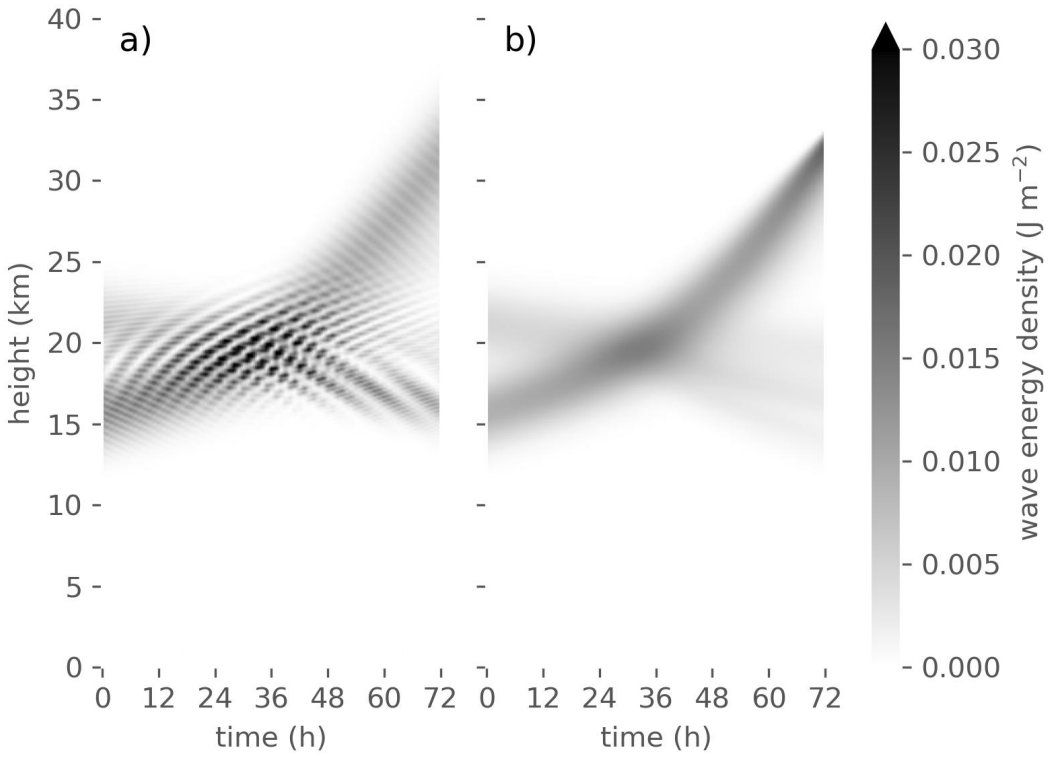


**FIGURE 4** Total wave energy density of simulations with  $\hat{m}_2 = 10$  and  $u_0 = 1 \text{ m s}^{-1}$ . The panels (a) and (b) depict the projected results for the wave-resolving and WKBJ simulations, respectively.

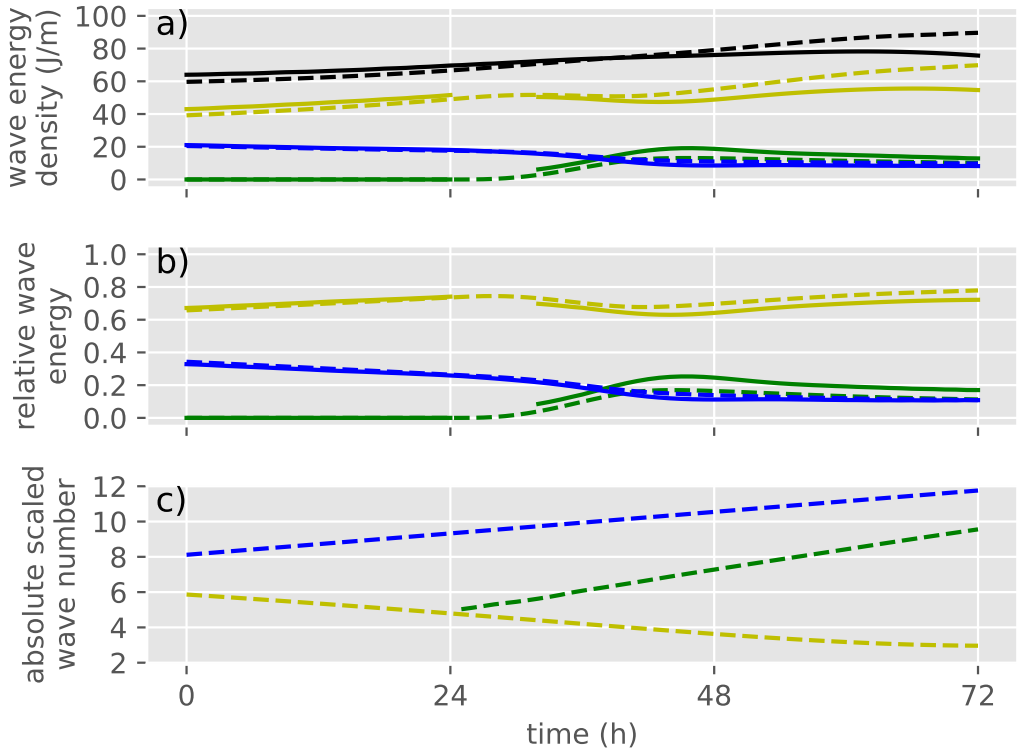


**FIGURE 5** Integrated wave energy densities of the separated wave trains in the simulations with  $\hat{m}_2 = 10$  and  $u_0 = 1 \text{ m s}^{-1}$ . Panels (a)-(c) show the absolute wave energy density, the relative wave energy density, and the mean absolute wavenumber, respectively. Solid lines correspond to the wave-resolving and dashed lines depict WKBJ simulation results. The black lines in panel (a) depicts the sum of the individual wave energy densities. The solid lines are broken where the wavelengths of the different wave trains have similar absolute values and can therefore not be separated.

474 shear but also due to the self-induced mean flow (Sutherland, 2006b). However, this effect is neglected in the WKBJ  
475 simulations, as it appears in the theory only at higher orders in the scale separation parameter,  $\epsilon$ . Moreover the scale  
476 separation assumption where  $\epsilon \rightarrow 0$  and the weak wave amplitude assumption (Eq. 7) are potential sources for errors.  
477 These systematic biases or other higher-order effects associated to wave modulation and not accounted for cause a  
478 mismatch in the evolution of the wave energy densities (Fig. 5a), particularly for  $t \geq 48$  h. To account for the effect  
479 of the modulation on the wave energy we normalize the individual wave energy densities by the total wave energy  
480 density, i.e. the sum of the individual wave energy densities (Fig. 5b). These relative wave energy densities show a  
481 qualitatively good agreement throughout the whole simulation - including the dynamics during the interaction at times  
482 from approximately 24 h to approximately 48 h. A closer look reveals, however, that the wave energy of the generated  
483 wave differs by up to 30 % relative to the LES (Fig. 5a and b). Possible reasons for this mismatch could be a systematic  
484 bias in the phases of the complex wave amplitudes introduced by the parametrization (cf. Section 6), inaccuracies  
485 of the parametrization parameter,  $\kappa$ , near  $\alpha = 0.1$  (cf. Fig. 1), or higher order modulation effects as discussed above.  
486 Despite this shortcoming the total energy exchange is well reproduced for various settings as discussed below. If, for  
487 example, one would consider an experiment with the same initial conditions but neglected wave-wave interaction, the  
488 superimposing wave trains would be modulated with constant wave action densities and not exchange any energy.  
489 In contrast, an experiment where the wave-mean-flow interaction is negligible, but the near resonant wave-wave  
490 interaction is included, would exhibit constant wave energies, but also no energy exchange, as it is the modulation  
491 which brings the waves into resonance. Note that where the absolute value of the wavelengths of the wave trains are  
492 too close (cf. Fig. 5c), a separation of the wave trains is numerically difficult and therefore omitted (cf. gaps in Fig. 5a  
493 and b).

494 Values of relative wave energy densities at the final time of the simulation serve as benchmark for comparisons in  
495 the further analysis of interaction simulations under varying conditions. In particular we consider varying background  
496 velocities as well as wave amplitudes (Figs. 6 to 8).



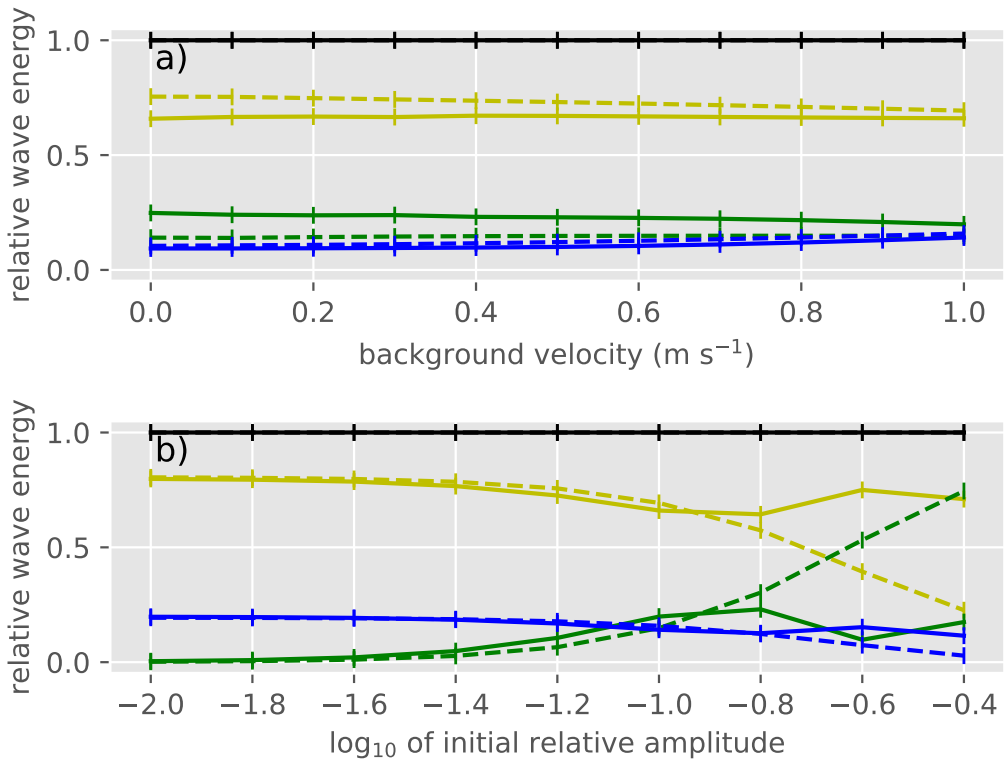


**FIGURE 6** Integrated relative wave energies per wave train at the end time of the simulations with non-dimensional vertical wavenumber  $\hat{m}_2 = 5$  and varying background velocity (a) as well as varying amplitude (b). While solid lines depict the wave-resolving simulations, dashed lines represent the corresponding WKBJ simulations.

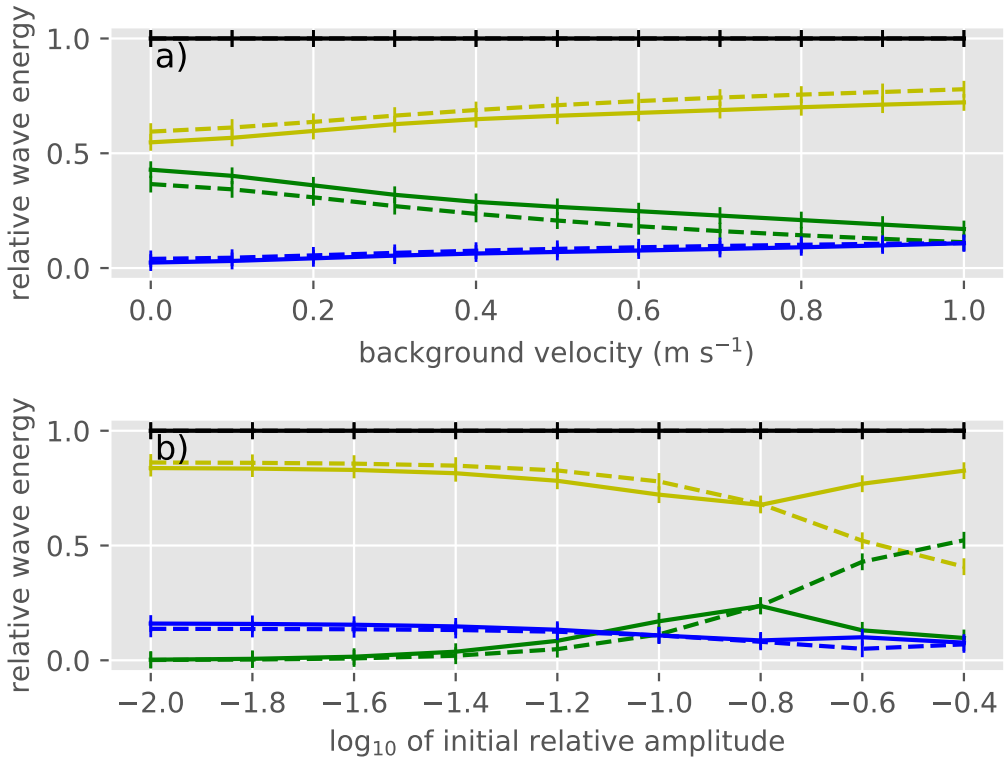


**FIGURE 7** Same as Fig. 6 for simulations with the non-dimensional vertical wavenumber  $\hat{m}_2 = 10$ .

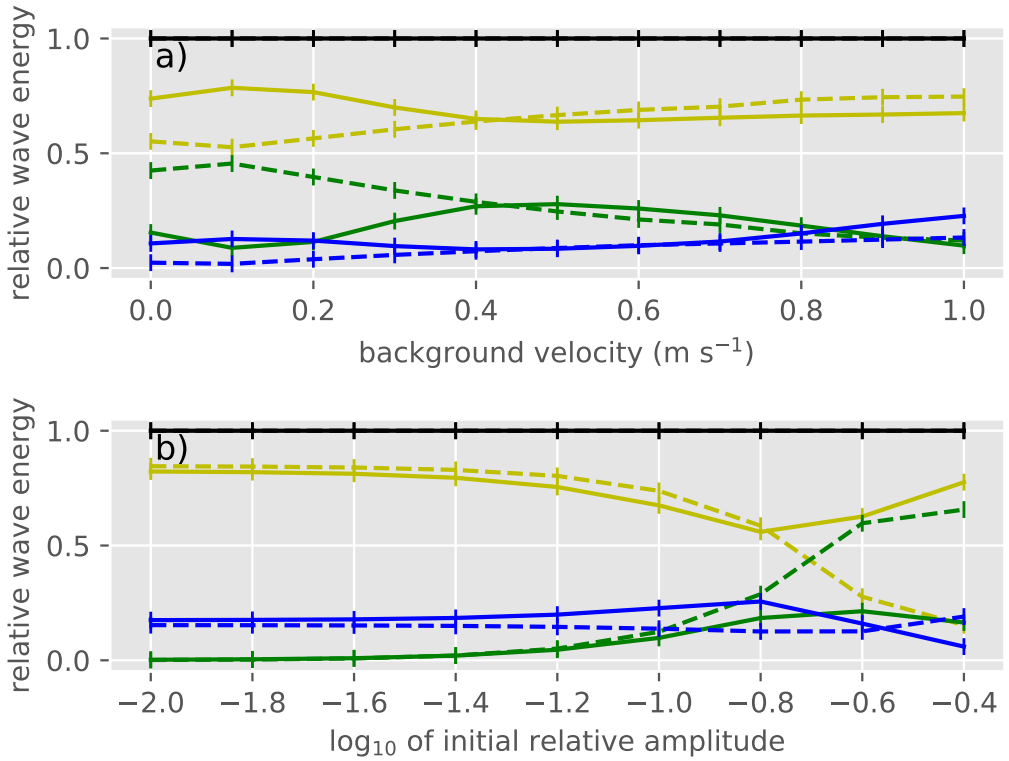


**FIGURE 8** Same as Fig. 6 for simulations with the non-dimensional vertical wavenumber  $\hat{m}_2 = 15$ .

## 497 7.4 | The Effect of the Wave Amplitudes

498 Varying the initial gravity wave amplitudes,  $\alpha$ , that is varying the strength of the nonlinearities relative to the modu-  
499 lation of the wave trains, we find good agreement for relative amplitudes smaller than  $\alpha = 10^{-1}$  (Figs. 6b, 7b, and 8b).  
500 As expected, the energy exchange increases with increasing amplitude as the nonlinearities are growing stronger. For  
501 amplitudes  $\alpha > 0.1$ , that is closer to the criterion of static instability, the WKBJ simulations fail to reproduce the wave-  
502 resolving simulations qualitatively and overestimate the triadic energy exchange. In general larger amplitudes may be  
503 subject to stronger nonlinear effects like self-acceleration, modulational instabilities, or overturning and turbulence  
504 (Sutherland, 2006a; Dosser and Sutherland, 2011; Bölöni et al., 2016). The wave-mean flow interactions, including  
505 the self-acceleration, are higher order effects in the WKBJ expansion and may be taken into account to improve the  
506 here presented method in the limit of larger amplitudes. As expected a WKBJ theory may not cover the break down  
507 of the wave trains at amplitudes near the static instability criterion unless using a suitable parameterization (Lindzen,  
508 1981; Bölöni et al., 2016). Also, the employed parameterization with a globally constant tuning parameter,  $\kappa$ , may  
509 lead to systematic biases at larger amplitudes (cf. Section 6).

510 In general wave amplitudes are modified through both triadic interactions and wave modulation (cf. Eqs. 22, 51,  
511 and 56). For small background flows  $u_0 \leq 1 \text{ m s}^{-1}$  the wave train evolution is dominated by triadic wave interactions  
512 and the amplitude variation due to wave modulation are comparatively small. Thus we do not correct the initial  
513 amplitudes with respect to the modulation while studying the influence of the wave amplitude and modulation on  
514 triadic interactions for  $u_0 \leq 1 \text{ m s}^{-1}$ . The wave amplitudes in Figs. 6 to 8 refer to the wave amplitudes in the initial  
515 conditions (cf. Eq. 84). For runs with strong background flows, i.e. where the evolution is dominated by the wave  
516 modulation, we correct the initial amplitude such that the wave amplitudes are comparable near resonance.

## 517 7.5 | The Effect of the Background Shear Strength

518 The wave modulation by the imposed background shear leads to a continuous spectral shift of the wavenumbers  
519 and frequencies. Effective energy exchange, however, is only possible near exact resonance. The resulting passage

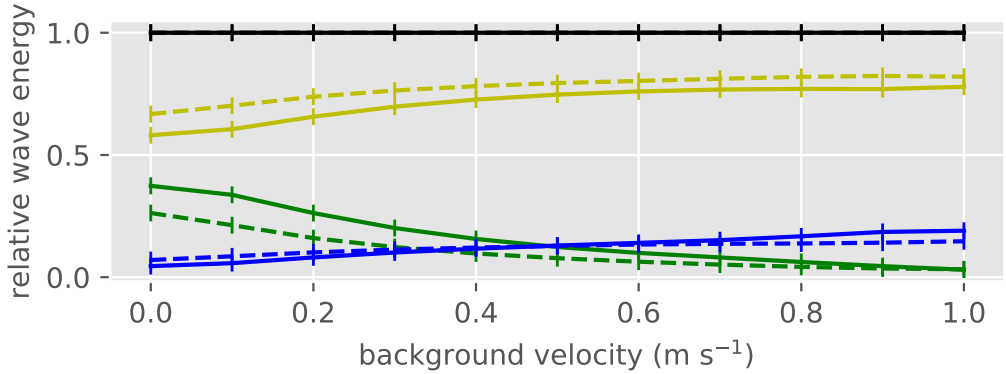


**FIGURE 9** Same as Fig. 8a for simulations with the non-dimensional vertical wavenumber  $\hat{m}_2 = 15$  and  $\alpha = 0.05$ .

520 through the resonance conditions therefore leads to a more localized interaction and limits the energy exchange. A  
 521 stronger background shear is associated with an increased modulation and thus generally leads to a reduction of the  
 522 energy exchange between the triad members. This effect is well reproduced in the here presented simulations for  
 523  $\hat{m}_2 = 5$ ,  $\hat{m}_2 = 10$ , and  $\hat{m}_2 = 15$  (Figs. Fig. 6a, 7a, and 8a) with a mismatch for large wavenumbers ( $\hat{m}_2 = 15$ ) and small  
 524 background velocities ( $u_0 \leq 0.4 \text{ m s}^{-1}$ ) (Fig. 8a).

525 For background velocity amplitudes smaller than  $u_0 = 0.5 \text{ m s}^{-1}$  the wave-induced mean flow (e.g. Sutherland,  
 526 2006b) in the wave-resolving simulations may lead to background shear strengths comparable to the imposed shear.  
 527 This shear consequently modulates the wave triads leading to a shift in wavenumbers and frequencies relative to the  
 528 WKBJ simulation where the effect is not included, as explained above. This effect, albeit small at small amplitudes,  
 529 may lead to significant differences between the wave-resolving simulations and the WKBJ simulation under conditions  
 530 where the spectral width of the triad resonance is small. Correspondingly, the mismatch between the simulations for  
 531 background flows,  $u_0 < 0.5 \text{ m s}^{-1}$ , at larger vertical wavenumbers,  $\bar{L}m_2 = 15$ , is believed to be caused by neglecting the  
 532 wave-mean-flow interactions in the present WKBJ theory (cf. Fig. 8a). In particular the self-induced wave modulation  
 533 perturbs the near-resonant interaction such that, even at small amplitudes, the energy exchange is limited due to  
 534 the frequency deviations. For comparison we repeat the experiment with varying background flows for  $\hat{m}_2 = 15$  but  
 535 decrease the amplitude to  $\alpha = 0.05$  (Fig. 9). Naturally at smaller amplitudes not only the triadic wave interaction  
 536 but also the self-induced wave modulation of the wave trains is reduced. Consequently the associated frequency

537 deviation from exact resonance is smaller. At the same time we find that the triad interaction is significantly stronger  
538 in the wave-resolving simulation despite the reduced nonlinearities at small imposed mean flows,  $u_0 < 0.5 \text{ m s}^{-1}$ . This  
539 qualitatively changed behavior of the wave-resolving simulation agrees well with the WKB prediction (Fig. 9).

540 Herein also lies a qualitative argument as to which non-linear effects dominate the wave evolution. At amplitudes  
541 near the static instability threshold all non-linear effects, like the here considered wave-wave interaction, the wave  
542 modulation by the mean-flow shear, or the here excluded self acceleration, are predicted to be equally important  
543 (Achatz et al., 2017). Reducing the amplitude, however, changes the picture. Using a weakly non-linear theory we find  
544 a regime where the wave modulation by the mean-flow shear and the wave-wave interactions dominate the dynamics  
545 while the self acceleration effect becomes a small correction (cf. Sections 2 and 5) which could be included into the  
546 theory by introducing an additional time and spatial scale (not shown). Also we have shown that at amplitudes  $\alpha \leq$   
547  $10^{-1}$  the employed parametrization is valid, however may produce systematic biases at larger amplitudes (cf. Section 6).  
548 Additionally we find the qualitative importance of various effects to be depend on the considered wave properties  
549 (cf. above). Consequently a quantitative mapping of the importance of the different non-linear effects is dependent  
550 on many variables and thus beyond the scope of this work.

## 551 7.6 | Energy Exchange at Strong Background Shear Flows

552 As explained above, background flows with stronger shear may lead to an increase in wave modulation and conse-  
553 quently a decrease in triadic wave interactions. To include values with shear strengths typical for atmospheric jet  
554 regions we augment our findings with WKB simulations for mean flow strengths up to  $u_0 = 9 \text{ m s}^{-1}$ . Those simula-  
555 tions confirm that for strong shear the simulation is dominated by wave modulation with small energy exchange due  
556 to triadic interactions (Fig. 10). While the evolution of the wave action density shows virtually no variations (Fig. 10a)  
557 the wave energy densities show strong variability due to the wave modulation (Fig. 10b). To estimate the strength of  
558 the wave interaction we repeat the simulations with disabled interaction scheme and then compare the two simula-  
559 tions. This allows us to we compute the fraction of energy transferred during the interaction. As a result we find that  
560 the transferred energy decreases systematically from values as high as 19% to well below 5% when increasing the

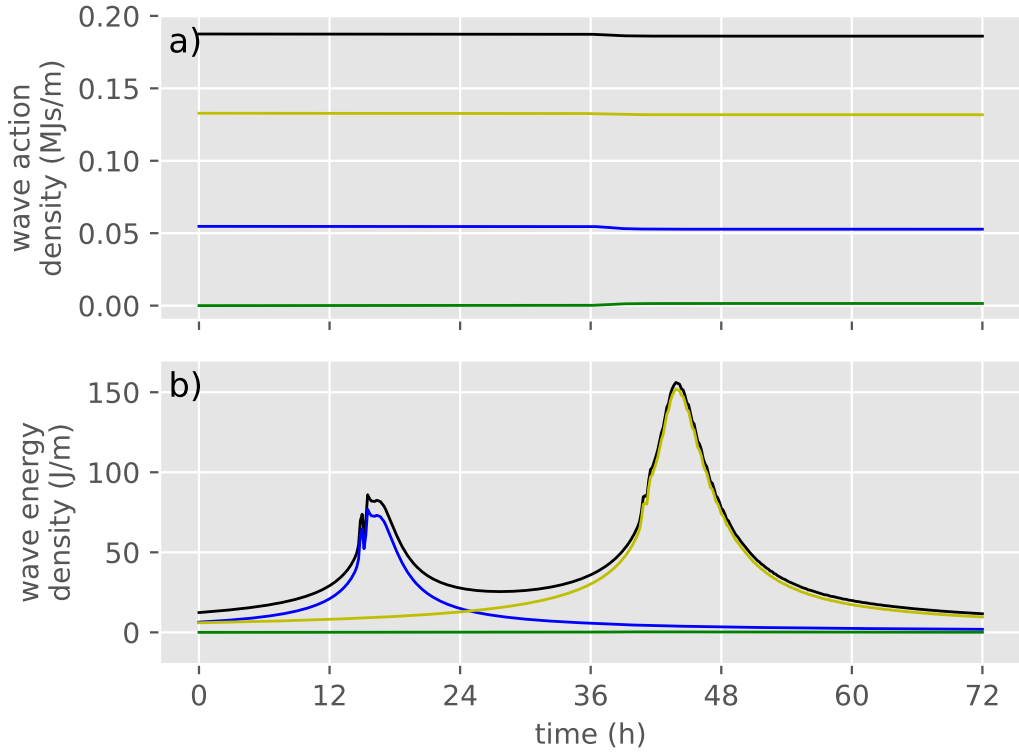


**FIGURE 10** Wave action- and energy densities of WKBJ simulations with  $u_0 = 9 \text{ m s}^{-1}$  as a function of time. While the evolution of the wave action densities is approximately constant (a), the wave energy densities are dominated by the wave modulation (b).

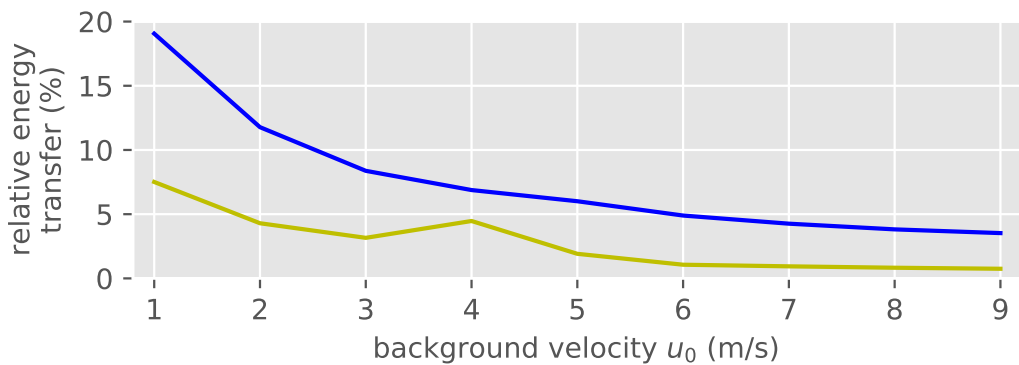


**FIGURE 11** Fraction of wave energy density of the initial wave trains transferred to a newly generated wave train as a function of background flow amplitude,  $u_0$ .

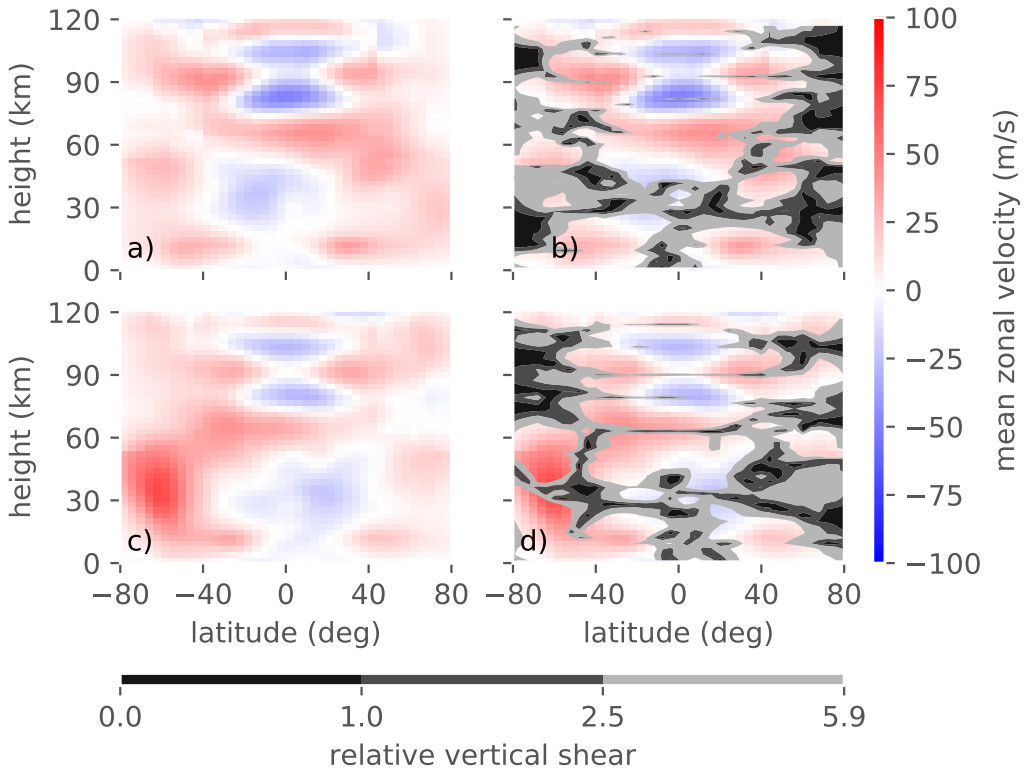


**FIGURE 12** Zonally and monthly averaged zonal velocities from the URAP data-set for March (a-b) and September (c-d). For comparison we show the vertical shear of the zonal velocity relative to the scaling of the idealized simulations,  $\frac{H}{2\pi u_0} \partial_z u$  with the reference values  $H = 40$  km, and  $u_0 = 1$   $\text{m s}^{-1}$  (b and d). The thresholds for the relative vertical shear correspond to energy transfer rates of 5% (5.9), 10% (2.5), and 19% (1) in the idealized simulations (cf. Fig. 11).



561 background amplitude from  $u_0 = 1 \text{ m s}^{-1}$  to  $u_0 = 9 \text{ m s}^{-1}$  (Fig. 11).

562 For a representative comparison with the atmosphere we consider the zonally averaged zonal velocity from the  
563 URAP climatology (Swinbank and Ortland, 2003) and its vertical shear. In particular during spring and autumn, after  
564 the break down of the polar night jet, we find large areas of relatively un-sheared zonal velocity in mid-latitude to  
565 sub-polar regions (Fig. 12a and c). For comparison we depict different vertical shear strengths as grey overlays that  
566 correspond to energy loss rates of  $> 19\%$  (black),  $10\%–19\%$  (grey), and  $5\%–10\%$  (light grey) in the idealized simulations  
567 (Figs. 11 and 12b and d). These reveal that large areas correspond to background flow shear strengths that permit  
568 for triadic wave-wave interactions without suppressing the spectral energy transfer due to wave modulation. We  
569 conclude that depending on the region and the season the gravity wave dynamics in the atmosphere is likely to be  
570 impacted by triadic wave-wave interactions.

## 571 8 | SUMMARY AND CONCLUSIONS

572 We have presented and applied a weakly nonlinear, Boussinesq theory of non-hydrostatic internal gravity waves (GWs)  
573 in a varying mean flow with constant stratification, extending previous work by Grimshaw (1988). The theory com-  
574 prises a superposition of wave trains whose amplitudes are modulated by a slowly varying background. There are  
575 three well-separated scales: the GW period and wavelength define the fast and short scales, the spatial scale of the  
576 mean flow represents the longest scales, and nonlinear GW-GW interactions act on intermediate scales. Away from  
577 resonance GWs follow linear WKBJ dynamics, characterized by short and long scales, and wave action is conserved.  
578 In resonance GWs depend on all three scales, and energy is exchanged between GWs in triadic interactions. Wave  
579 amplitudes are weak so that GWs are still well-defined, including dispersion and polarization relations, and there is no  
580 leading-order impact on the mean flow. The modulation by the mean flow permanently changes the GW wavenum-  
581 bers so that they are brought by this process into and out of resonance. This adds an additional source of spectral and  
582 spatial variability not accounted for in theories without a varying mean flow, like wave-turbulence approaches (e.g.  
583 Nazarenko, 2011).

584 For a numerical implementation of this theory we have supplemented a spectral ray-tracing code (Muraschko  
585 et al., 2015) by a wave-wave-interaction module. Consistent with the two scaling regimes a parameterization for  
586 an effective spectral resonance width has been developed, allowing for fully resonant interaction within a spectral  
587 resonance window. Beyond the corresponding spectral resonance threshold the wave triad members stop interacting  
588 and follow linear WKBJ dynamics. The universal resonance threshold is adaptive to changes in triad wavenumbers as  
589 well as background shear strengths and therefore applicable for a wide range of wavenumbers and background shear.  
590 Only for wave amplitudes near the threshold of static instability systematic biases may occur, possibly exacerbated by  
591 the so-far neglect of a direct, non-dissipative, transient GW impact on the mean flow, which has been shown by Bölöni  
592 et al. (2016) to potentially be as important as impacts by wave dissipation. We believe this is the first implementation  
593 of interacting internal gravity wave triads into a WKBJ ray tracer taking into account the modulation of the waves by  
594 a slowly varying background.

595 The supplemented WKBJ code is validated against simulations from a wave resolving model. In all cases con-  
596 sidered wave amplitudes and mean flow have been assumed to be horizontally homogeneous. Two wave packets  
597 are considered that generate a third one while spectrally passing through resonance for a range of vertical scales.  
598 Comparing the WKBJ ray-tracing simulations with corresponding wave-resolving simulations we generally find good  
599 qualitative and quantitative agreement for the wave modulation and triadic interactions, provided the wave amplitude  
600 with respect to static instability does not exceed 0.1. It is clear, however, that beyond this limit direct, non-dissipative  
601 GW-mean-flow interactions are not negligible anymore.

602 Depending on the strength of the mean-flow shear two interesting regime limits emerge: On the one hand, in  
603 weak shear and at large vertical wavenumbers nonlinear effects become visible that lead to differences between  
604 wave-resolving and WKBJ simulations. It is very well possible that this is due to the self-induced mean wind that the  
605 present WKBJ implementation does not take into account. In strong background shears, on the other hand, wave-  
606 wave interactions seem to become partially suppressed by the wave modulation on account of the mean flow. This  
607 is due to both the corresponding strong changes in wave energy density and the more rapid development of the  
608 GW wavenumbers, so that the time window for resonant triad interactions is narrower. Hence an eventual outcome  
609 of further studies of GW-GW interactions in the atmosphere might well be that wave modulation dominates the

610 evolution of the GW spectrum in strongly sheared regions, such as jet streams, while triadic interactions dominantly  
611 shape the GW spectrum in more weakly sheared regions, such as the mid-latitudes and polar regions during spring  
612 after the breakdown of the polar night jet. There, however, the modulation of GW-GW interactions by the self-induced  
613 mean wind could be non-negligible, a process not taken into account by wave turbulence theory.

614 Obviously there still is some way to go until this picture is confirmed. Both varying stratification and rotation  
615 will have to be included into theory and numerical implementation. Compressibility effects should be considered, but  
616 most pressing seems to be an inclusion of the GW impact on the mean flow. While atmospheric winds are clearly  
617 horizontally inhomogeneous GW parameterizations are typically single column implementations and do not take into  
618 account the lateral propagation of realistic internal gravity wave packets. Yet, a three-dimensional implementation  
619 of a WKB ray tracer could potentially carry over the concepts for the wave-wave interaction applied here with an  
620 accordingly adapted strategy for the ray tracing geometry. It would also be of interest to consider clusters of GW-GW  
621 interactions with common triad members (cf. Walsh and Bustamante, 2020), and validate the approach against these.  
622 Finally, a challenge will be continuous GW spectra. Our theory still assumes that the GW spectrum has distinct peaks  
623 that are sufficiently separated to allow for the discretely polychromatic GW fields considered here. Smoother spectra  
624 will need further theoretical developments, that however seem to be worth the effort.

## 625 **Acknowledgements**

626 GV thanks the German Research Foundation (DFG) for partial support through the research unit *Multiscale Dynamics*  
627 *of Gravity Waves (MS-GWaves)* and through grants AC 71/10-2 and BO 5071/1-2. UA thanks the German Research  
628 Foundation (DFG) for partial support through the research unit *Multiscale Dynamics of Gravity Waves (MS-GWaves)*  
629 and through grants AC 71/8-2, AC 71/9-2, AC 71/10-2, AC 71/11-2, and AC71/12-2. TA was funded by the US  
630 National Science Foundation through the grant 631 DMS-1512925. Furthermore he thanks the Goethe-University  
631 Frankfurt as well as the Wilhelm-Else-Heraeus Foundation for their support through a guest professorship. Calcula-  
632 tions for this research were conducted on *Goethe-HLR Cluster*.

## 633 A | NOTES ON THE IMPLEMENTATION IN A RAY-TRACING MODEL

634 The numerical implementation of the WKB theory for interacting internal gravity waves comes with various difficul-  
 635 ties. At the same time it is crucial for the usage of the insights for future studies. We therefore outline our solution  
 636 strategy for a one-dimensional spectral ray-tracing model (Muraschko et al., 2015) in the following three sections.

### 637 A.1 | Spectral Ray Tracing

638 Using a Lagrangian ray-tracing technique (Muraschko et al., 2015), the code predicts the development of a spectral  
 639 wave action density,  $\mathcal{N}(z, \mathbf{k}, t)$ , depending on vertical position,  $z$ , wavenumber,  $\mathbf{k} = \mathbf{k}_h + m\mathbf{e}_z$ , decomposed into its  
 640 horizontal part,  $\mathbf{k}_h$ , and the vertical wavenumber,  $m$ , and time. In the triad cases discussed here it peaks in wavenumber  
 641 space at the three contributing wavenumbers and its wavenumber integral yields the superposition of the spatial wave  
 642 action densities appearing in the theory derived here, i.e.

$$\int d^3k \mathcal{N}(z, \mathbf{k}, t) = \sum_{\beta} \mathcal{A}_{\beta}(z, t) \quad (86)$$

643 The corresponding prognostic equation is, outside of the triad-resonance regime,

$$\frac{D_r \mathcal{N}}{Dt} = 0 \quad (87)$$

644 where

$$\frac{D_r}{Dt} = \frac{\partial}{\partial t} + c_{g,z} \frac{\partial}{\partial z} + \dot{m} \frac{\partial}{\partial m} \quad (88)$$

645 is a material derivative. Here  $c_{g,z}$  is the vertical group velocity of a spectral component and  $\dot{m}$  is the rate by which the  
 646 vertical wavenumber, and hence also frequency and group velocity, changes in response to vertical derivatives in the  
 647 resolved horizontal flow. Because of the assumed horizontal homogeneity of wave amplitudes and mean flow, their  
 648 is no movement in  $k_h$ -subspace. The model allows a GW impact on the resolved flow, given by

$$\left( \frac{\partial U}{\partial t} \right)_{\text{gw}} = - \frac{\partial}{\partial z} \int d^3 k c_{g,z} k_h \mathcal{N} \quad (89)$$

649 which is, however, neglected here, due to the weak-amplitude assumption of our theoretical setup. The numerical  
 650 discretization uses a decomposition of that part of phase space, spanned by  $x$  and  $k$ , with non-zero  $\mathcal{N}$  into rectangular  
 651 ray volumes. These ray volumes propagate through phase space, with velocities  $c_{g,z}$  and  $\dot{m}$  that typically distort the  
 652 ray volumes - while keeping their volume content - as well as displace them, and only in the wave-resonance regime  
 653 their wave-action density is changed. Further details are given by Muraschko et al. (2015).

## 654 A.2 | Gapless Wave Trains

655 In the original implementation described by Muraschko et al. (2015) each ray volume is displaced in  $z$  following the  
 656 group velocity of its central carrier ray. For its displacement in  $m$  the wave-number velocities  $\dot{m}$  are determined at  
 657 its  $m$ -edges, with same position in  $z$  as the carrier ray, yielding on top of the  $m$ -displacement also a change in the  
 658 ray volume width  $\Delta m$  in  $m$ . Because the volume content must be unchanged, the vertical width of the ray volume

659 is then adjusted so that  $\Delta m \Delta z$  does not change. In this procedure, ray volumes initially adjacent in  $z$  may begin to  
660 overlap or drift apart at later integration times - the representation of initially continuous wave trains may become  
661 fragmented. Triadic interactions, however, depend on the spatial overlay of the triad members and therefore suffer  
662 from reduced interaction within the gaps of a wave train using this approach. To resolve these discontinuities we  
663 consider two carrier rays per ray volume which are initially located at the central wavenumber but on the upper  
664 and lower boundary. Advancing the two carrier rays allows for the ray volume to shear in spectral direction due to  
665 a height-dependent background shear. Consequently the ray volume's vertical wavenumber comprises a gradient in  
666 height. The corresponding group velocities of the two carrier rays are used to displace the upper and lower boundaries,  
667 and  $\Delta m$  is adjusted so that the phase space volume content remains unchanged.

### 668 A.3 | Interaction Between Ray Volumes

669 Both position as well as the spatial extent of the ray volumes rarely coincide. Hence, special care has to be taken where  
670 interacting ray volumes overlap partially. Our implementation of the triadic interaction into the ray tracer therefore  
671 relies on a chain of geometric operations.

672 First all spatially overlapping pairs of ray volumes are tested for possible resonances making use of the resonance  
673 threshold defined in Eq. (82). For simplicity and based on the knowledge about the chosen initial conditions we  
674 restrict the identification of resonant pairs here to a sum interactions. However, this assumption may be easily relaxed  
675 to both sum and difference interactions. Note that single ray volumes may be in resonance with several other ray  
676 volumes due to partial overlaps. Based on the identified resonance pairs the interacting ray volumes (parent rays)  
677 are split such that a minimum set of vertical layers with full overlap can be considered for the energy exchange.  
678 The corresponding central carrier wavenumbers are deduced from the linear interpolation between the values on  
679 the boundaries (cf. Appendix A.2). In each vertical interaction level the identified sum interaction also defines an  
680 interaction volume bounded by the vertical bounds of the slab and the maximum spectral deviation allowed, based on  
681 the interaction threshold. In particular the minimum wavenumber,  $m'_1$ , and maximum wavenumber,  $m''_1$ , are derived

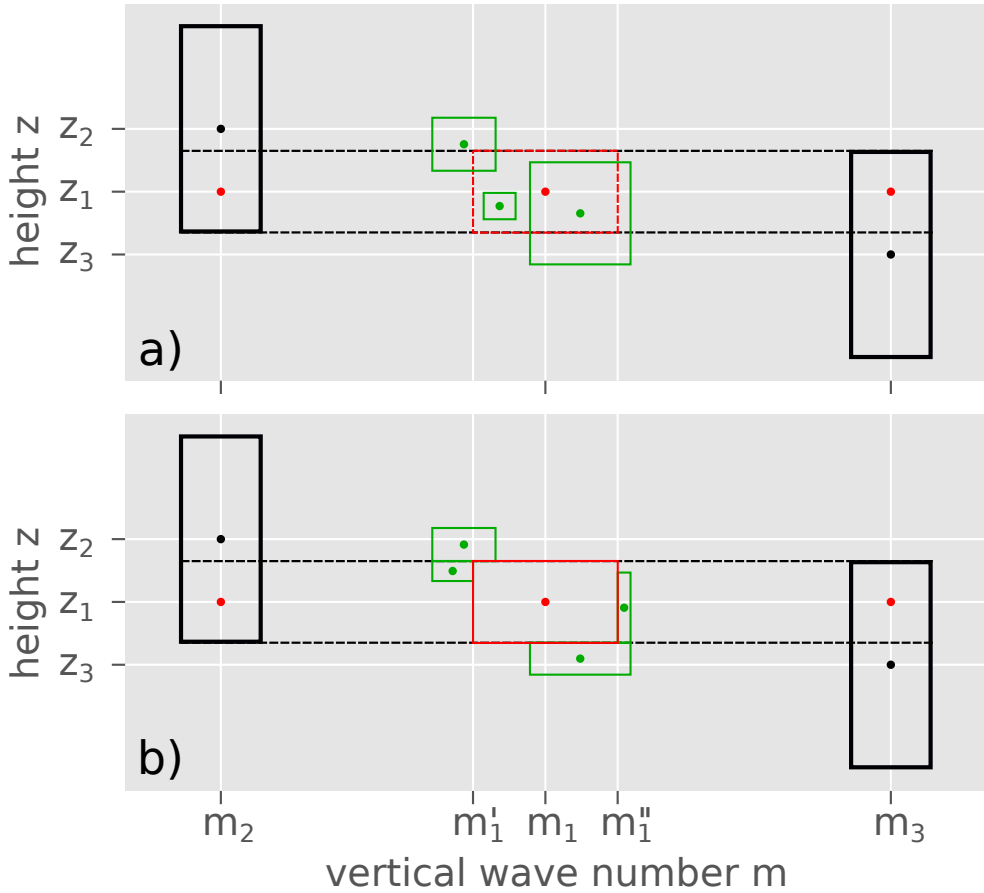


**FIGURE 13** Schematic of the geometry between interacting wave triads. While the black rectangles depict the parent ray volumes the red and green rectangles represent the interaction volume and existing ray volumes overlapping with the interaction volume, respectively. The central dots represent the central carrier rays. All ray volumes are first split based on the vertical overlap and the spectral resonance threshold (a). Consecutively all ray volumes overlapping with the resonance volume are unified into a single ray volume filling the entire interaction volume (b).

682 from the condition

$$\left| \frac{\hat{\omega}_2 + \hat{\omega}_3 - \hat{\omega}_1}{\hat{\omega}_2 + \hat{\omega}_3} \right| = \left| 1 - \frac{\hat{\omega}_1(k_2 + k_3, m_1)}{\hat{\omega}_2 + \hat{\omega}_3} \right| \leq R^\dagger \quad (90)$$

683 where we know that the resonance conditions are fulfilled exactly in the horizontal such that  $k_1 = k_2 + k_3$ . In other  
 684 words the spectral interaction threshold also defines the spectral window with which a resonant pair can exchange  
 685 energy. Within this interaction volume all existing ray volumes are split and unified into a single ray volume which  
 686 then forms the third triad member. This geometry is visualized in Fig. 13. Consecutively all triads can be advanced  
 687 in time using the interaction equations (Eq. 59) with the dephasing exponential replaced by unity as explained in  
 688 Section 6. The equations are advanced using a third-order Runge-Kutta scheme equivalent to the time integration of  
 689 the wavenumbers and positions. Note that in order to derive the wave amplitude from the wave action density (cf. Eq.  
 690 22) the phase of the corresponding complex wave amplitude is needed. Therefore the phases of the complex wave  
 691 amplitudes which are associated to the ray volumes must be stored and applied accordingly. These phases may be  
 692 set to a vertically constant value at initial times but are modified during the interaction steps. An initially zero-valued  
 693 complex amplitude has an initially undefined phase, which can be chosen arbitrarily. As a result of the nonlinear  
 694 interaction, this phase acquires a defined value in subsequent time steps as the amplitude becomes non-zero. Finally,  
 695 the resulting wave action changes are deduced from the integrated amplitudes and all initially split parent rays are  
 696 reunified.

697 This procedure generates a large number of small ray volumes around the interaction volumes in each time step.  
 698 Introducing merging schemes for these ray volumes may therefore greatly reduce memory usage, output data size, and  
 699 computation time. The here presented solution strategy can be used for a range of applications. Triadic interactions  
 700 with a modulating background shear (cf. Section 7) or a variable background stratification as well as phase resolving  
 701 simulations with zero background flows are among the use cases.



702 **references**

- 703 Achatz, U., Klein, R. and Senf, F. (2010) Gravity waves, scale asymptotics and the pseudo-incompressible equations. *Journal*  
704 *of Fluid Mechanics*, **663**, 120–147.
- 705 Achatz, U., Ribstein, B., Senf, F. and Klein, R. (2017) The interaction between synoptic-scale balanced flow and a finite-  
706 amplitude mesoscale wave field throughout all atmospheric layers: weak and moderately strong stratification. *Quarterly*  
707 *Journal of the Royal Meteorological Society*, **143**, 342–361.
- 708 Böllöni, G., Ribstein, B., Muraschko, J., Sgoff, C., Wei, J. and Achatz, U. (2016) The Interaction between Atmospheric Gravity  
709 Waves and Large-Scale Flows: An Efficient Description beyond the Nonacceleration Paradigm. *Journal of the Atmospheric*  
710 *Sciences*, **73**, 4833–4852.
- 711 Borchert, S., Achatz, U. and Fruman, M. D. (2014) Gravity wave emission in an atmosphere-like configuration of the differen-  
712 tially heated rotating annulus experiment. *Journal of Fluid Mechanics*, **758**, 287–311.
- 713 Bretherton, F. P. (1966) The propagation of groups of internal gravity waves in a shear flow. *Quarterly Journal of the Royal*  
714 *Meteorological Society*, **92**, 466–480.
- 715 Bustamante, M. D. and Kartashova, E. (2009) Effect of the dynamical phases on the nonlinear amplitudes' evolution. *EPL*, **85**.
- 716 Caillol, P. and Zeitlin, V. (2000) Kinetic equations and stationary energy spectra of weakly nonlinear internal gravity waves.  
717 *Dynamics of Atmospheres and Oceans*, **32**, 81–112.
- 718 Callies, J., Ferrari, R. and Bühler, O. (2014) Transition from geostrophic turbulence to inertia-gravity waves in the atmospheric  
719 energy spectrum. *Proceedings of the National Academy of Sciences*, **111**, 17033–17038.
- 720 Danilov, V. G. (2001) Weak asymptotics method. *arXiv:math-ph*, **0105025v1**, 1–15.
- 721 Dewan, E. M. and Good, R. E. (1986) Saturation and the 'universal' spectrum for vertical profiles of horizontal scalar winds in  
722 the atmosphere. *Journal of Geophysical Research*, **91**, 2742–2748.
- 723 Dong, B. and Yeh, K. C. (1988) RESONANT AND NONRESONANT WAVE-WAVE INTERACTIONS IN AN ISOTHERMAL  
724 ATMOSPHERE. *Journal of Geophysical Research*, **93**, 3729–3744.
- 725 – (1991) On nonresonant interactions of atmospheric waves in a rotating earth. *Physica Scripta*, **43**, 534–544.
- 726 Dosser, H. V. and Sutherland, B. R. (2011) Anelastic internal wave packet evolution and stability. *Journal of the Atmospheric*  
727 *Sciences*, **68**, 2844–2859.

- 728 Eckermann, S. D. and Marks, C. J. (1997) GROGRAT: A new model of the global propagation and dissipation of atmospheric  
729 gravity waves. *Advances in Space Research*, **20**, 1253–1256.
- 730 Eden, C., Chouksey, M. and Olbers, D. (2019) Mixed Rossby-Gravity Wave-Wave Interactions. *Journal of Physical Oceanography*,  
731 **49**, 291–308.
- 732 Elipot, S., Lumpkin, R. and Prieto, G. (2010) Modification of inertial oscillations by the mesoscale eddy field. *Journal of Geo-*  
733 *physical Research: Oceans*, **115**, C09010.
- 734 Fritts, D. C. and Alexander, M. J. (2003) Gravity wave dynamics and effects in the middle atmosphere. *Reviews of Geophysics*,  
735 **41**, 1/1003.
- 736 Fritts, D. C., Shaojian Sun and Ding-Yi Wang (1992) Wave-wave interactions in a compressible atmosphere 1. A general  
737 formulation including rotation and wind shear. *Journal of Geophysical Research*, **97**, 9975–9988.
- 738 Fritts, D. C. and Vanzandt, T. E. (1993) Spectral estimates of gravity wave energy and momentum fluxes. Part I: energy dissi-  
739 pation, acceleration, and constraints. *Journal of the Atmospheric Sciences*, **50**, 3685–3694.
- 740 Garrett, C. and Munk, W. (1972) Space-Time scales of internal waves. *Geophysical Fluid Dynamics*, **3**, 225–264.
- 741 – (1975) Space-Time of Internal Waves: A progress report. *Journal of Geophysical Research*, **80**, 291–297.
- 742 Glebov, S., Kiselev, O. and Vladimir, L. (2005) Slow Passage through Resonance for a Weakly Nonlinear Dispersive Wave. *SIAM*  
743 *Journal on Applied Mathematics*, **65**, 2158–2177.
- 744 Grimshaw, R. (1975) Nonlinear internal gravity waves in a rotating fluid. *Journal of Fluid Mechanics*, **71**, 497–512.
- 745 – (1988) Resonant wave interactions in a stratified shear flow. *Journal of Fluid Mechanics*, **190**, 357–374.
- 746 Grimshaw, R. H. (1977) The Modulation of an Internal Gravity-Wave Packet, and the Resonance with the Mean Motion. *Studies*  
747 *in Applied Mathematics*, **56**, 241–266.
- 748 Hasselmann, K. (1962) On the non-linear energy transfer in a gravity-wave spectrum: Part 1. General theory. *Journal of Fluid*  
749 *Mechanics*, **12**, 481–500.
- 750 – (1966) Feynman diagrams and interaction rules of wave-wave scattering processes. *Reviews of Geophysics*, **4**, 1–32.
- 751 Huang, K. M., Zhang, S. D. and Yi, F. (2007) A numerical study on nonresonant interactions of gravity waves in a compressible  
752 atmosphere. *Journal of Geophysical Research Atmospheres*, **112**, D11115.

- 753 Kim, Y., Eckermann, S. D. and Chun, H. Y. (2003) An overview of the past, present and future of gravity-wave drag parametriza-  
754 tion for numerical climate and weather prediction models. *Atmosphere - Ocean*, **41**, 65–98.
- 755 Kim, Y.-H., Bölöni, G., Borchert, S., Chun, H.-Y. and Achatz, U. (2020) Towards transient subgrid-scale gravity wave represen-  
756 tation in atmospheric models. Part II: Wave intermittency simulated with convective sources. *Journal of the Atmospheric*  
757 *Sciences*, 1–49.
- 758 Lindzen, R. S. (1981) Turbulence and stress owing to gravity wave and tidal breakdown. *Journal of Geophysical Research*, **86**,  
759 9707–9714.
- 760 Lvov, Y. V., Polzin, K. L. and Tabak, E. G. (2004) Energy spectra of the ocean's internal wave field: theory and observations.  
761 *Physical review letters*, **92**, 128501.
- 762 Lvov, Y. V. and Tabak, E. G. (2001) Hamiltonian formalism and the garrett-munk spectrum of internal waves in the ocean.  
763 *Physical Review Letters*, **87**, 168501.
- 764 McComas, C. H. and Bretherton, F. P. (1977) Resonant interaction of oceanic internal waves. *Journal of Geophysical Research*,  
765 **82**, 1397–1412.
- 766 McEwan, A. D. and Plumb, R. A. (1977) Off-resonant amplification of finite internal wave packets. *Dynamics of Atmospheres*  
767 *and Oceans*, **2**, 83–105.
- 768 Mueller, P. (1976) On the diffusion of momentum and mass by internal gravity waves. *Journal of Fluid Mechanics*, **77**, 789–823.
- 769 Mueller, P., Holloway, G., Henyey, F. and Pomphrey, N. (1986) Nonlinear interactions among internal gravity waves. *Reviews*  
770 *of Geophysics*, **24**, 493–536.
- 771 Muraschko, J., Fruman, M. D., Achatz, U., Hickel, S. and Toledo, Y. (2015) On the application of Wentzel-Kramer-Brillouin  
772 theory for the simulation of the weakly nonlinear dynamics of gravity waves. *Quarterly Journal of the Royal Meteorological*  
773 *Society*, **141**, 676–697.
- 774 Nazarenko, S. (2011) *Lecture Notes in Physics Vol 825: Wave Turbulence*, vol. 825 of *Lecture Notes in Physics*. Berlin, Heidelberg:  
775 Springer Berlin Heidelberg.
- 776 Nelder, J. A. and Mead, R. (1965) A Simplex Method for Function Minimization. *The Computer Journal*, **7**, 308–313.
- 777 Neu, J. (1983) Resonantly Interacting Waves. *SIAM Journal on Applied Mathematics*, **43**, 141–156.

- 778 Olbers, D. and Eden, C. (2013) A Global Model for the Diapycnal Diffusivity Induced by Internal Gravity Waves. *Journal of*  
779 *Physical Oceanography*, **43**, 1759–1779.
- 780 Olbers, D. J. (1976) Nonlinear energy transfer and the energy balance of the internal wave field in the deep ocean. *Journal of*  
781 *Fluid Mechanics*, **74**, 375–399.
- 782 Plougonven, R. and Zhang, F. (2014) Internal gravity waves from atmospheric jets and fronts. *Reviews of Geophysics*, **52**, 33–76.
- 783 Polzin, K. L. and Lvov, Y. V. (2011) Toward regional characterizations of the oceanic internal wavefield. *Reviews of Geophysics*,  
784 **49**, RG4003.
- 785 Pomphrey, N., Meiss, J. D. and Watson, K. M. (1980) Description of nonlinear internal wave interactions using Langevin  
786 methods. *Journal of Geophysical Research*, **85**, 1085–1094.
- 787 Quinn, B., Eden, C. and Olbers, D. (2020) Application of the IDEMIX concept for Internal Gravity Waves in the Atmosphere.  
788 *Journal of the Atmospheric Sciences*, **77**, 1–59.
- 789 Rieper, F., Achatz, U. and Klein, R. (2013a) Range of validity of an extended WKB theory for atmospheric gravity waves:  
790 One-dimensional and two-dimensional case. *Journal of Fluid Mechanics*, **729**, 330–363.
- 791 Rieper, F., Hickel, S. and Achatz, U. (2013b) A conservative integration of the pseudo-incompressible equations with implicit  
792 turbulence parameterization. *Monthly Weather Review*, **141**, 861–886.
- 793 Senf, F. and Achatz, U. (2011) On the impact of middle-atmosphere thermal tides on the propagation and dissipation of gravity  
794 waves. *Journal of Geophysical Research Atmospheres*, **116**.
- 795 Smith, S. A., Fritts, D. C. and VanZandt, T. E. (1987) EVIDENCE FOR A SATURATED SPECTRUM OF ATMOSPHERIC GRAVITY  
796 WAVES. *Journal of the Atmospheric Sciences*, **44**, 1404–1410.
- 797 Sutherland, B. R. (2006a) Internal wave instability: Wave-wave versus wave-induced mean flow interactions. *Physics of Fluids*,  
798 **18**, 074107.
- 799 – (2006b) Weakly nonlinear internal gravity wavepackets. *Journal of Fluid Mechanics*, **569**, 249–258.
- 800 – (2010) *Internal Gravity Waves*. Cambridge, UK: Cambridge University Press.
- 801 Swinbank, R. and Ortland, D. A. (2003) Compilation of wind data for the Upper Atmosphere Research Satellite (UARS) Refer-  
802 ence Atmosphere Project. *Journal of Geophysical Research: Atmospheres*, **108**, 4615.

- 803 Walsh, S. G. and Bustamante, M. D. (2020) On the convergence of the normal form transformation in discrete Rossby and  
804 drift wave turbulence. *Journal of Fluid Mechanics*, **884**, A28.
- 805 Wilhelm, J., Akylas, T. R., Bölöni, G., Wei, J., Ribstein, B., Klein, R. and Achatz, U. (2018) Interactions between Meso- and Sub-  
806 Mesoscale GravityWaves and their Efficient Representation in Mesoscale-Resolving Models. *Journal of the Atmospheric  
807 Sciences*, **75**, 2257–2280.
- 808 Yi, F. and Xiao, Z. (1997) Evolution of gravity waves through resonant and nonresonant interactions in a dissipative atmosphere.  
809 *Journal of Atmospheric and Solar-Terrestrial Physics*, **59**, 305–317.